Article

Parkinson's disease as a somato-cognitive action network disorder

https://doi.org/10.1038/s41586-025-10059-1

Received: 30 October 2024

Accepted: 15 December 2025

Published online: 04 February 2026

Open access

Check for updates

Jianxun Ren[1,33]✉, Wei Zhang[1,2,33], Louisa Dahmani[3,4], Evan M. Gordon[5,6], Shenshen Li[1,7], Ying Zhou[1,8], Yang Long[1,8], Jianting Huang[1], Yafei Zhu[1,2], Ning Guo[1], Changqing Jiang[9], Feng Zhang[9], Yan Bai[10], Wei Wei[10], Yaping Wu[10], Alan Bush[4,11], Matteo Vissani[4,11], Luhua Wei[12], Carina R. Oehrn[13], Melanie A. Morrison[14,15], Ying Zhu[1], Chencheng Zhang[16,17], Qingyu Hu[1], Yilin Yin[1], Weigang Cui[1], Xiaoxuan Fu[1], Ping Zhang[1], Weiwei Wang[1], Gong-Jun Ji[18,19,20], Ji He[1,21], Kai Wang[19,20], Dongsheng Fan[21], Zhaoxia Wang[12], Teresa Kimberley[3,22,23], Simon Little[15,24,25], Philip A. Starr[13,15,25], Robert Mark Richardson[4,11], Luming Li[9,26], Meiyun Wang[10,27]✉, Danhong Wang[1]✉, Nico U. F. Dosenbach[5,6,28,29,30,31] & Hesheng Liu[1,32]✉

Parkinson's disease (PD) is an incurable neurological disorder that often begins insidiously with sleep disturbances and somatic symptoms, progressing to whole-body motor and cognitive symptoms[1–5]. Dysfunction of the somato-cognitive action network (SCAN)—which is thought to control action execution[6,7] by coordinating arousal, organ physiology and whole-body motor plans with behavioural motivation—is a potential contributor to the diverse clinical manifestations of PD. To investigate the role of the SCAN in PD pathophysiology and treatments (medications, deep-brain stimulation (DBS), transcranial magnetic stimulation (TMS) and MRI-guided focused ultrasound stimulation (MRgFUS)), we built a large (n = 863), multimodal, multi-intervention clinical imaging dataset. Resting-state functional connectivity revealed that the substantia nigra and all PD DBS targets (subthalamic nucleus, globus pallidus and ventral intermediate thalamus) are selectively connected to the SCAN rather than to effector-specific motor regions. Importantly, PD was characterized by specific hyperconnectivity between the SCAN and the subcortex. We therefore followed six PD cohorts undergoing DBS, TMS, MRgFUS and levodopa therapy using precision resting-state functional connectivity and electrocorticography recording. Efficacious treatments reduced SCAN-to-subcortex hyperconnectivity. Targeting the SCAN instead of effector regions doubled the efficacy of TMS treatments. Focused ultrasound treatment benefits increased when the target was closer to the thalamic SCAN sweet spot. Thus, SCAN hyperconnectivity is central to PD pathophysiology and its alleviation is a hallmark of successful neuromodulation. Targeting functionally defined subcortical SCAN nodes may improve existing therapies (DBS, MRgFUS), whereas cortical SCAN targets offer effective non-invasive or minimally invasive neuromodulation for PD.

PD, classically recognized as a movement disorder, manifests not as the dysfunction of specific motor effectors but as a systemic disruption that affects the entire body, including difficulties with gait (for example, postural instability, gait slowness)[8–10], tremor, rigidity and incoordination[11,12]. Beyond motor symptoms, PD is associated with a variety of non-motor symptoms such as dysautonomia (for example, constipation, orthostatic hypotension)[3–5,13], sleep disturbances (for example, rapid-eye-movement-onset sleep disorder)[1], and the slowing and diminishment of voluntary behaviour (for example, bradykinesia, abulia, apathy, executive dysfunction)[14]. PD motor symptoms are modifiable by cognitive factors; for example, walking may worsen under time pressure but improve when listening to music[15], tremor may amplify with increased cognitive load[16], and sudden bursts of rapid movement can occur during emergencies[17].

The pathophysiological hallmark of PD is the degeneration of dopaminergic neurons in the substantia nigra (SN)[1,3,18], leading to dysfunction within a cortico–basal ganglia–thalamic circuit comprised of the subthalamic nucleus (STN), ventral intermediate nucleus/centromedian nucleus of the thalamus (VIM/CM), globus pallidus internus (GPi) and externus (GPe), putamen and primary motor cortex (M1)[5,19], revealed by electrophysiological and functional/metabolic neuroimaging evidence[3,20–23]. This cortico–subcortical circuit is initially responsive to dopaminergic medications, particularly levodopa, which effectively control motor symptoms in the early stage of the disease[1,3,24]. However, over time, treatment efficacy may wane or be complicated by motor fluctuations and dyskinesias, prompting the need for adjunctive therapies, such as invasive or non-invasive neuromodulation[25,26]. The US Food and Drug Administration (FDA) has approved DBS of the STN and

A list of affiliations appears at the end of the paper.

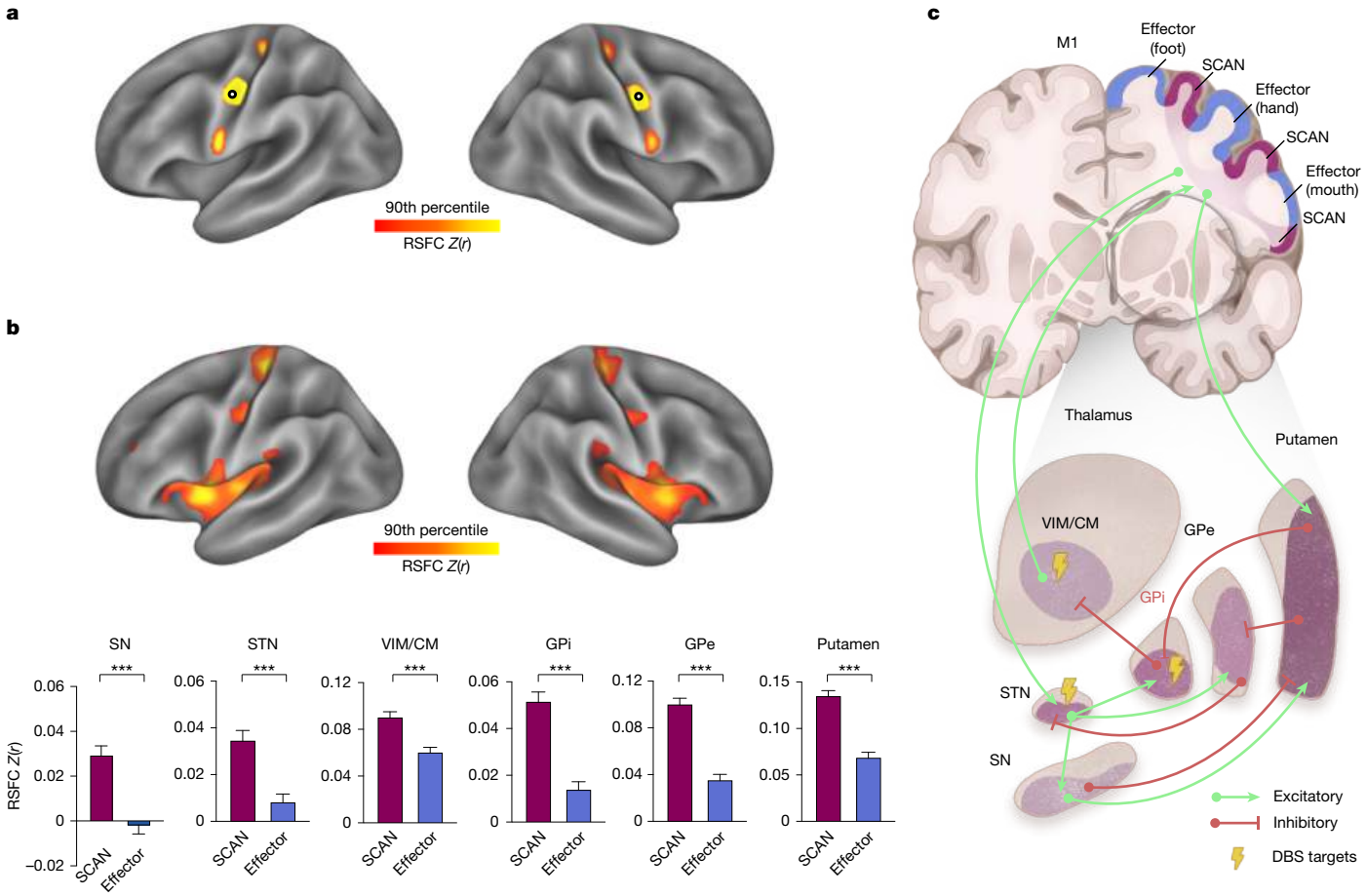

Fig. 1 | Cortical functional connectivity of six subcortical regions critical in PD. a, Seed-based RSFC ($Z(r)$) mapping revealed the SCAN motif with three distinct intereffector regions in the primary motor (M1) strip, using a large sample of patients with PD (PIPD dataset, $n = 166$). Group-averaged RSFC maps in patients with PD and HC individuals, as well as individual-specific maps are provided in Extended Data Fig. 1. **b**, The average RSFC map across six subcortical nodes in the PD circuit (SN, STN, VIM/CM, GPi, GPe and putamen) shows selective functional connectivity to the SCAN in patients with PD. For each subcortical node, the bar plots demonstrate significantly stronger connectivity within the SCAN than in effector-specific (foot, hand, mouth) regions (bottom; two-tailed paired-sample t-tests, FDR corrected, $P = 1.43 \times 10^{-24}$ (SN), $P = 2.97 \times 10^{-18}$ (STN), $P = 6.10 \times 10^{-20}$ (VIM/CM), $P = 2.55 \times 10^{-25}$ (GPi), $P = 6.34 \times 10^{-39}$ (GPe), $P = 6.79 \times 10^{-39}$ (putamen)). Data are mean ± s.e.m. See Extended Data Fig. 2 for node-specific RSFC maps, including midline views. Supplementary Fig. 1 shows the stronger subcortex-to-SCAN RSFC than subcortex-to-effector RSFC in HC individuals (all $P < 0.001$, PIPD dataset, $n = 60$). **c**, Illustration of the cortico–subcortical circuit that is important in PD, comprising the SCAN and six subcortical nodes. Newly recognized SCAN regions (purple) are interposed among effector-specific motor regions (blue) within the M1 (ref. 6). The green and red lines represent excitatory and inhibitory projections, respectively. The cortico–STN projection indicates the hyperdirect pathway. FDA-approved DBS targets for PD treatment are highlighted, including the STN, GPi and VIM. A version of the illustration with additional detail is provided in Supplementary Fig. 3. ***$P < 0.001$.

GPi for various motor symptoms, and DBS of the VIM for tremor[26,27]. DBS efficacy has improved with adaptive stimulation protocols[28] and advanced neuroimaging[29], but existing targets have shown limited success in improving levodopa-resistant freezing of gait and may lead to adverse effects, such as cognitive impairment[26,30]. Moreover, access to DBS is restricted by its invasiveness and high costs[25,26]. Non-invasive approaches such as TMS have also shown therapeutic effect but remain underexplored[31], possibly due to the lack of precise targets in the cortex[25].

Historically, the complex action, arousal, autonomic and volitional symptoms of PD were difficult to explain by dysfunction of effector-specific (foot, hand, mouth) motor regions[18]. The recent discovery and subsequent verification that SCAN regions, responsible for action implementation, axial movement, arousal and autonomic control, alternate with classical effector-specific primary motor regions along the central sulcus updated our understanding of the brain's motor systems[6,7,32–36]. As PD's action, motor, somatic, arousal and cognitive symptoms are not effector specific, but are multidomain and affect the whole body, SCAN dysfunction might contribute to its pathophysiology, and therefore SCAN-specific neuromodulation might help to treat its symptoms[37,38].

To investigate these possibilities, we built a large ($n = 863$), multimodal, multi-intervention clinical imaging dataset (a list of datasets is provided in Extended Data Table 1). To characterize resting-state functional connectivity (RSFC) in PD, we used our precision imaging PD (PIPD; $n = 166$ individuals with PD; $n = 60$ healthy control (HC) individuals) and DBS sweet spot (DBS-SS; $n = 342$) datasets[39]. To examine the specificity of the RSFC findings observed in PD, we included three additional movement disorder cohorts as controls: essential tremor (ET; $n = 45$ patients), dystonia ($n = 42$ patients, $n = 21$ HC individuals) and amyotrophic lateral sclerosis (ALS; $n = 30$ patients, $n = 30$ HC individuals). To test and track treatment effects, we followed six different patient cohorts undergoing DBS (DBS-functional magnetic resonance imaging (fMRI) dataset: $n = 14$ patients with PD, $n = 25$ HC individuals; DBS-electrocorticography (ECoG) dataset: $n = 17$ patients with PD), adaptive DBS (aDBS; $n = 4$ patients with PD), TMS ($n = 36$ patients with PD), MRgFUS ($n = 10$ patients with PD) and levodopa challenge test (LCT dataset: $n = 21$ patients

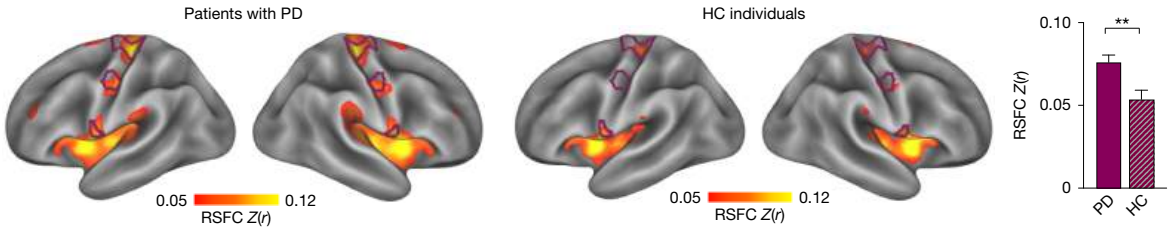

Fig. 2 | Cortico–subcortical SCAN hyperconnectivity in PD. The average RSFC map across the six PD-relevant subcortical nodes (SN, STN, VIM, GPi, GPe and putamen) in 65 patients with PD, who were sampled from 166 patients to match HC individuals (left). The SCAN regions are indicated by purple borders (Methods). The average RSFC map across 60 HC individuals exhibits a similar spatial pattern (middle), but with relatively weaker RSFC to the SCAN. The bar plot on the right shows the average functional connectivity between subcortical nodes and the SCAN, which was significantly higher in patients with PD than in HC individuals (two-tailed independent *t*-test, $t = 3.2$, $^{**}P = 0.002$; PIPD dataset, $n = 65$ (PD), $n = 60$ (HC)). Data are mean ± s.e.m. See Extended Data Fig. 3 for node-specific maps and Supplementary Fig. 6 for replication in the DBS-fMRI dataset.

with PD) with RSFC precision functional mapping[40–47] and ECoG recordings.

Key subcortical nuclei in PD link to the SCAN

We evaluated cortico–subcortical circuitry with RSFC. The distinctive SCAN pattern (SCAN detection is described in the Methods), which alternates with foot, hand, mouth motor regions along the central sulcus, was evident in both patients with PD and HC individuals (Fig. 1a and Extended Data Fig. 1; PIPD: $n = 226$). Critically, six subcortical structures (SN, STN, VIM/CM, GPi, GPe and putamen) of which the involvement in PD has been established[3,19] were all more strongly connected with the SCAN than with effector-specific (foot, hand, mouth) motor regions and other functional networks (Fig. 1b, Extended Data Fig. 2 and Supplementary Figs. 1 and 2; all two-tailed paired $t > 9.8$, $P < 0.0001$, false-discovery rate (FDR) corrected). These results indicated that the cortico–basal ganglia–thalamic circuit that is important in PD is preferentially SCAN connected rather than motor effector connected (Fig. 1c).

SCAN hyperconnectivity in PD

We examined circuit dysfunction in PD (a subset of the PIPD dataset; $n = 65$ patients with PD and $n = 60$ age-matched control individuals) and found that the RSFC between the SCAN and the six subcortical structures (SN, STN, VIM, GPi, GPe, putamen) was significantly elevated in patients with PD compared with in HC individuals (Fig. 2; two-tailed independent $t = 3.2$, $P = 0.002$). Specifically, cortical SCAN regions were significantly hyperconnected with the SN, STN, GPe and putamen in patients (all two-tailed independent $t > 2.3$, all $P \leq 0.022$, FDR corrected; Extended Data Fig. 3). The observed SCAN hyperconnectivity in PD was successfully replicated in the full samples of the PIPD dataset (two-tailed independent $t = 3.5$, $P < 0.001$) and the DBS-fMRI dataset (Supplementary Fig. 6; two-tailed independent $t = 2.4$, $P = 0.020$; PD, $n = 14$; HC, $n = 25$). This hyperconnectivity coincides with the expansion of SCAN territory in PD in all six subcortical nodes (two-tailed χ^2 tests, $P < 0.001$, FDR corrected), as revealed by a winner-takes-all parcellation (Extended Data Fig. 5). Importantly, this hyperconnectivity was specific to the SCAN and was not observed in other canonical functional networks (Supplementary Fig. 4; all $P > 0.05$, FDR corrected). Relative hyperconnectivity was also observed in the metabolic network-based PD-related pattern (PDRP)[20,22,23] that partially overlaps with the SCAN (Supplementary Fig. 5). Moreover, SCAN hyperconnectivity was absent in three other movement disorders used as control conditions: ET, dystonia and ALS (Extended Data Fig. 4), indicating that, although SCAN hyperconnectivity may not be unique to PD, it is not a feature that is shared across all movement disorders. Furthermore, significant associations were observed between subcortex-to-SCAN RSFC and motor symptoms (Supplementary Fig. 7; Movement Disorder Society-Unified Parkinson's Disease Rating Scale Part III (MDS-UPDRS-III), Pearson's $r = 0.162$, $P = 0.037$), cognition (Mini-Mental State Examination (MMSE), $r = 0.161$, $P = 0.038$), anxiety (Hamilton Anxiety Rating Scale (HAMA), $r = -0.186$, $P = 0.017$) and depression (Hamilton Depression Rating Scale (HAMD), $r = -0.177$, $P = 0.023$).

Effective DBS in PD targets the SCAN

To test whether DBS for PD selectively modulates the SCAN circuit, we first confirmed that effective DBS lead locations (that is, sweet spots; Methods) within the STN, GPi and VIM (DBS-SS dataset, $n = 342$) were more strongly connected with the SCAN than with primary motor effectors (all two-tailed paired $t > 13.5$, all $P < 0.0001$, FDR corrected; Extended Data Fig. 6, Supplementary Fig. 8 and Supplementary Table 1). We next examined data from 17 patients with PD who underwent single-pulse STN-DBS with ECoG recordings in the M1 (DBS-ECoG dataset[48]; Fig. 3a and Supplementary Fig. 9). When the motor subregion of the STN was stimulated, more of the responsive ECoG electrodes with the strongest evoked potentials were found in probabilistically defined SCAN regions than in effector-specific motor regions (two-tailed χ^2 test, $P < 0.001$; Fig. 3b, Methods and Supplementary Fig. 9c). Responsive electrodes in the mouth effector region were also closer to the border with the SCAN, away from the centre of the effector-specific region (Fig. 3b). Moreover, the average ECoG trace across responsive electrodes in the SCAN showed significantly greater voltage amplitudes than electrodes in the M1 effector region (mouth) at most of the timepoints (80.0% of time) within the 10-ms post-stimulation window (cluster-based permutation tests, $P < 0.05$, cluster-level multiple-comparison corrected; Fig. 3c and Supplementary Fig. 9d). The selective connectivity between the STN treatment target and the SCAN was further confirmed by the first cortical evoked potential (P1), which is the first positive voltage peak occurring at least 2 ms after stimulation onset and corresponds to the antidromic activation of the monosynaptic hyperdirect pathway from cortex to the STN[48]. We found that the P1 amplitude in the SCAN was significantly greater than that in M1 effector regions (two-tailed independent $t = 5.7$, $P = 1.33 \times 10^{-6}$ (Fig. 3c); all $P \leq 0.001$ for different thresholds (Supplementary Fig. 9d)). Furthermore, in four individuals who underwent aDBS treatment (aDBS dataset; Extended Data Table 1), the cortical electrodes selected to record stimulation-entrained biomarkers of motor fluctuations for adaptive STN-DBS[28] were positioned closer to the centre of the most superior SCAN node than to the centres of the hand and foot motor regions (Extended Data Fig. 7). Thus, RSFC and ECoG data indicate that STN regions effectively modulated by DBS are functionally connected to the SCAN rather than to the effector-specific motor cortex, and recordings from areas proximal to the SCAN provide reliable control signals for aDBS.

Treatments reduce SCAN hyperconnectivity

We tested whether DBS normalizes the cortico–subcortical SCAN hyperconnectivity observed in patients with PD. In the longitudinal

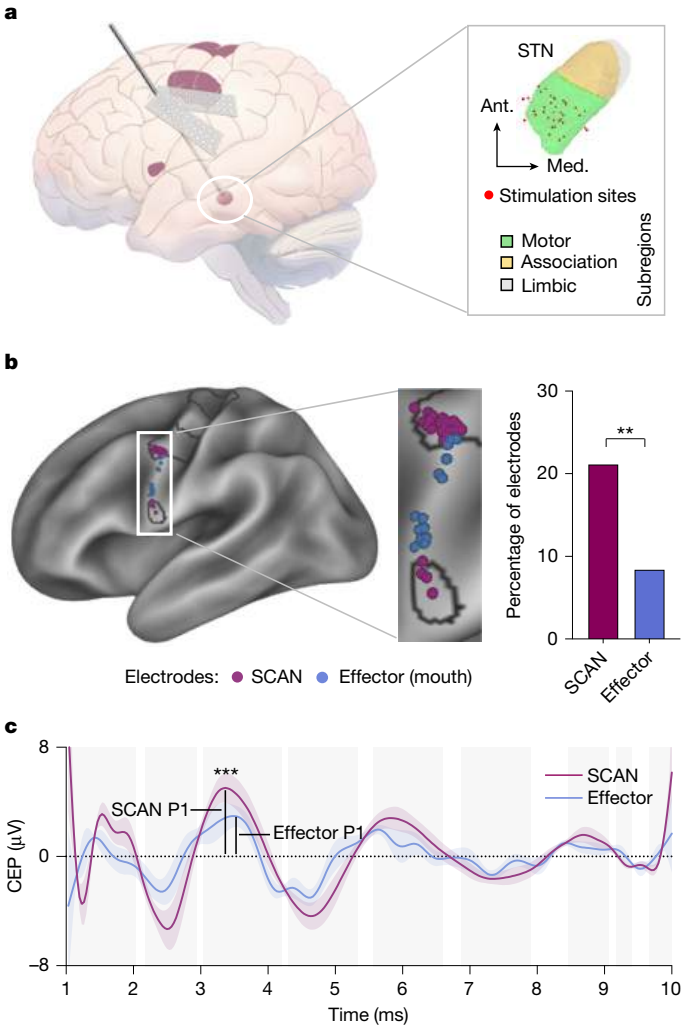

Fig. 3 | DBS-evoked cortical responses in the SCAN. a, ECoG electrodes were placed over the motor cortex during the STN-DBS surgery to record cortical responses evoked by STN stimulation (DBS-ECoG dataset, $n = 17$, total of 284 ECoG electrodes). Stimulation sites (red dots) localized in the motor subregion (green) of the STN were retained for subsequent analyses (Methods and Supplementary Fig. 4). Ant., anterior; med., medial. **b**, The top 15% most DBS-responsive electrodes in the M1 are plotted on the cortical surface; the purple and blue dots represent electrodes within the SCAN and effector motor region (mouth), respectively. The black boundary shows the SCAN regions. The proportion of the responsive electrodes located in the SCAN is significantly higher than that in the effector region (two-tailed χ^2 test; $^{**}P = 0.0021$). The findings were consistent across various electrode selection thresholds, ranging from the top 10% to top 50% most-responsive electrodes. **c**, Cortical evoked potentials (CEP) of responsive electrodes. Average ECoG traces across the top 20 most-responsive electrodes within each network show significantly stronger activity in the SCAN than in the mouth network at 80.0% of the timepoints within the 10-ms recording time window. The shaded areas around the curves indicate the s.d. The background grey shaded areas denote significant differences (cluster-based permutation tests, $P < 0.05$). Specifically, the P1 amplitude, denoted by vertical lines, was significantly greater in the SCAN than in the mouth network (two-tailed independent t-test, $^{***}P = 1.13 \times 10^{-5}$). The findings were robust across different thresholds, ranging from 10 to 50 responsive electrodes (all $P \leq 0.001$). Results for alternative thresholds are shown in Supplementary Fig. 9.

DBS-fMRI dataset ($n = 14$; Supplementary Table 2), we first confirmed that the volume of tissue activated (VTA) by bilateral STN stimulation (Fig. 4a) overlapped with the STN sweet spot from the DBS-SS dataset (Fig. 4b; Dice coefficient = 74.3%). Motor symptoms, as measured by UPDRS-III total scores, were significantly improved at 1, 3, 6 and 12 months after DBS surgery compared with at the presurgical baseline (Fig. 4c; linear mixed-effects (LME) model, main effect of time, $F = 15.71$, $P < 0.0001$; all one-tailed paired $t > 2.8$, all $P < 0.008$, FDR corrected). At the presurgical baseline, patients with PD exhibited significant hyperconnectivity between the subcortex and the SCAN cortical regions compared with the HC individuals (two-tailed independent $t = 2.4$, $P = 0.020$; Fig. 4d,e), replicating the results from the PIPD dataset (Fig. 2). This SCAN hyperconnectivity was successfully attenuated across longitudinal follow-ups after STN-DBS (LME model, main effect of time, $F = 4.25$, $P = 0.006$), with significant decreases at the 1-month, 6-month and 12-month follow-up timepoints (all one-tailed paired $t > 1.8$, all $P < 0.05$, FDR corrected) and a modest reduction at the 3-month timepoint (one-tailed paired $t = 1.5$, $P = 0.077$, FDR corrected). However, STN-DBS did not result in any significant changes in subcortex-to-effector RSFC (LME model, main effect of time, $F = 1.73$, $P = 0.16$; Supplementary Fig. 10). To further validate this effect, we performed an additional analysis comparing DBS on versus off states using only postoperative data. Consistent with the longitudinal findings, subcortex-to-SCAN RSFC was significantly lower during the DBS on condition than during the DBS off state (LME model, $F = 7.87$, $P = 0.006$; Supplementary Fig. 11), while RSFC with other functional networks remained unchanged (LME models, all $P > 0.05$). Moreover, changes in STN-SCAN RSFC after DBS surgery, across multiple follow-up visits, were significantly associated with improvements in UPDRS-III scores (LME model, $F = 6.86$, $P = 0.013$; Supplementary Fig. 12). These results suggest that STN-DBS acts on the PD circuit by specifically downregulating SCAN hyperconnectivity.

Moreover, we examined whether effective dopaminergic medication also normalizes SCAN hyperconnectivity. In a simplified LCT (Methods and Supplementary Table 3), patients with PD showed a significant improvement in motor symptoms after medication (Extended Data Fig. 8a; one-tailed paired $t = 7.18$, $P < 0.0001$). Importantly, SCAN hyperconnectivity was significantly reduced by levodopa (Extended Data Fig. 8b; one-tailed paired $t = 3.58$, $P = 0.001$), suggesting that dopaminergic therapy and neuromodulation act on the SCAN to alleviate PD motor symptoms.

Modulating the SCAN improves outcomes

Given that effective DBS targets are specifically connected to the SCAN cortical regions (Figs. 1b and 4e and Extended Data Fig. 6), non-invasive neuromodulation targeting cortical SCAN nodes may similarly reduce hyperconnectivity and improve PD symptoms[25,38]. We therefore tested whether repetitive TMS (rTMS) targeting the SCAN would lead to better motor outcomes than targeting the M1 effector regions in PD. Thirty-six patients with PD were randomly assigned to either the SCAN ($n = 18$) or the effector ($n = 18$) targeting group (Fig. 5a), and received 2-week intermittent theta-burst stimulation (iTBS) rTMS intervention (Fig. 5b,c and Supplementary Fig. 16; the patient-specific targeting procedure is described in the Methods). There were no significant differences in demographics or baseline clinical symptoms between the two groups (Supplementary Tables 4 and 5). Patients, assessors and TMS operators were blinded to the group allocations. During and after the treatment regimen (protocol details are provided in the Methods and Supplementary Fig. 13), both groups exhibited significant alleviation of motor symptoms, as evidenced by reductions in MDS-UPDRS-III scores compared with the baseline (LME model, mean differences for SCAN group: week 1, −8.54, 95% confidence interval (CI) = −10.89 to −6.19; week 2, −13.48, 95% CI = −15.83 to −11.13; effector group: week 1, −4.14, 95% CI = −6.55 to −1.72; week 2, −6.49, 95% CI = −8.91 to −4.07; Fig. 5d and Supplementary Table 6). However, the SCAN group demonstrated significantly greater symptom reduction than the effector group at both week 1 and 2 (post hoc comparisons, both $P < 0.012$, Bonferroni correction) and faster symptom relief (LME model, group-by-time interaction, $P < 0.001$). The subgroup analysis stratified by the most

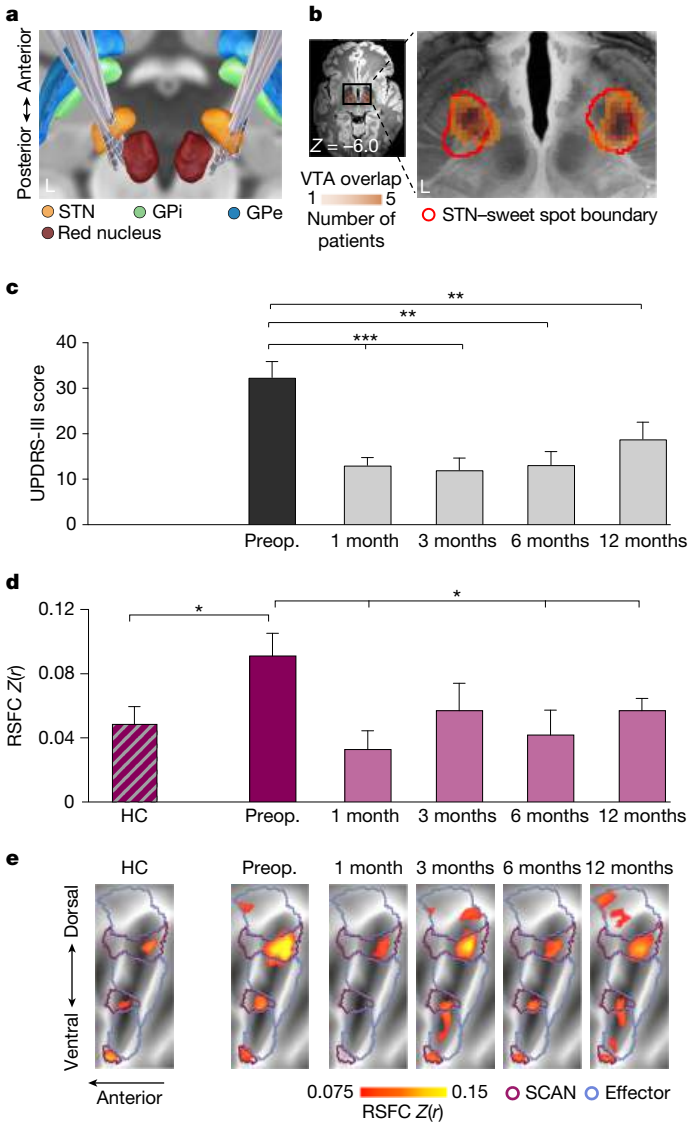

Fig. 4 | Effects of STN-DBS on SCAN hyperconnectivity in PD. a, Electrode lead placements for all 14 patients with PD in the DBS-fMRI dataset are presented alongside the surrounding subcortical nuclei. Bilateral STN (orange), GPi (green), GPe (blue) and the red nucleus (dark red) are shown. **b**, The VTA of STN-DBS across all patients (orange) showed 74.3% overlap with the STN sweet spot from the DBS-SS dataset (red outline). **c**, Clinical improvements due to STN-DBS. The symptom severity measured by MDS-UPDRS-III total scores is presented, showing scores preoperatively (preop., black bar) and at 1, 3, 6 and 12 months after STN-DBS surgery (grey bars). The scores are significantly lower at all follow-up points compared with at the baseline ($n = 14$; all FDR-corrected one-tailed paired $t > 2.8$, all $P < 0.008$). Data are mean ± s.e.m. **d**, Functional connectivity of the subcortex to the SCAN during STN-DBS. The RSFC strength between the subcortical regions of the PD circuit and the SCAN is shown for HC individuals ($n = 25$; striped bar), patients with PD ($n = 14$) before surgery (purple bar), and at four follow-up timepoints after STN-DBS (pink bars). Patients with PD had a significantly stronger RSFC than the HC individuals before surgery (one-tailed independent t-test, $^*P = 0.020$). Postoperative RSFC strength significantly or modestly decreased compared with the preoperative levels (one-tailed paired-sample t-tests, FDR corrected). Data are mean ± s.e.m. **e**, Functional connectivity of subcortical PD circuitry to the M1. Group-average cortical functional connectivity maps are displayed on flattened representations of M1 surfaces. In general, connectivity is stronger with the SCAN (purple) than with effector-specific motor regions (blue). Before surgery, patients exhibited hyperconnectivity within the SCAN compared with the HC individuals. After STN-DBS, connectivity levels became more like those of HC individuals across all follow-up periods. $^*P < 0.05$, $^{**}P < 0.01$.

affected limb (upper versus lower) showed consistent effects (Supplementary Fig. 14). The SCAN group showed significantly larger and/or faster reductions of bradykinesia (LME model, main effect of group, $P = 0.033$; group-by-time interaction, $P = 0.043$), rigidity (main effect of group, $P = 0.027$; group-by-time interaction, $P = 0.044$), tremor (main effect of group, $P = 0.030$), and axial symptoms (LME model, main effect of group, $P = 0.040$) compared with the effector group (Supplementary Fig. 15 and Supplementary Table 6). Targeted rTMS of the SCAN regions reduced cortico–subcortical SCAN hyperconnectivity (week 2 versus baseline: one-tailed paired $t = 2.29$, $P = 0.020$; Fig. 5c), but did not change subcortex-to-effector RSFC ($t = 0.45$, $P = 0.320$; Supplementary Fig. 16a), consistent with the specific normalization effect on SCAN hyperconnectivity observed in our DBS-fMRI dataset (Fig. 4d,e) and LCT dataset (Extended Data Fig. 8). The cortico–subcortical SCAN hyperconnectivity reduction was significantly greater in the SCAN group than in the effector group (LME model, group-by-time interaction, $F = 4.48$, $P = 0.044$; Supplementary Fig. 16b). Nevertheless, the therapeutic potential of SCAN-targeted rTMS in PD, as suggested by this small, single-centre study, should be further tested in larger, multicentre trials.

The VIM is the main target for tremor alleviation in tremor-dominant PD[49,50]. As the VIM is preferentially connected with the SCAN, we examined the potential of using the SCAN circuit to guide focused ultrasound thalamotomy in the MRgFUS dataset. In ten patients who underwent MRgFUS thalamotomy of the VIM contralateral to the most affected hand[49], we identified the centre of the SCAN's functional representation in the thalamus as the hypothesized optimal target for each patient (Methods and Extended Data Fig. 9). The Euclidean distance between the optimal SCAN targets and actual targets was significantly anticorrelated with motor symptom improvement (MDS-UPDRS-III change score, Spearman correlation, $\rho = -0.68$, $P = 0.031$). By contrast, the distance to motor effector-specific hotspots (also defined by RSFC) and the VIM sweet spot in the thalamus did not show significant correlations with symptom improvement (Spearman correlations, all $\rho > -0.24$, all $P > 0.488$). These results indicate that lesions made closer to the SCAN hotspot in the central thalamus provide better clinical outcomes, suggesting that MRgFUS treatment might be optimized in individual patients by localizing the target based on the SCAN-to-thalamus RSFC.

SCAN as the core circuit in PD

The subcortical SCAN-connected regions have critical roles in information integration for the purpose of rapid action[51,52], consistent with the proposed functions of the SCAN[6]. The cortico–subcortical SCAN circuit is ideally situated to integrate motor planning and execution, autonomic and physiological functions, and other relevant internal and external signals[6,7,32,33,53,54] to guide goal-directed behaviour[36,55,56]. PD, which manifests with non-effector-specific motor symptoms, motor initiation and coordination deficits, as well as with physiological and autonomic dysfunction[4], is characterized by SCAN dysregulation. Currently available circuit therapeutics (STN-, GPi-, VIM-DBS and VIM-MRgFUS) all target regions within this SCAN circuit and modulate the cortical SCAN regions, as evidenced by our DBS-ECoG (Fig. 3), DBS-fMRI (Fig. 4 and Extended Data Fig. 6), aDBS (Extended Data Fig. 7) and MRgFUS (Extended Data Fig. 9) data. Selectively targeting SCAN regions with rTMS proved to be more effective in alleviating symptoms compared with targeting M1 effector regions, and it reduced SCAN hyperconnectivity similar to the effects of DBS (Fig. 5). Further characterization of SCAN and related circuitry should lead to a deeper understanding of the pathogenesis of PD and further optimization of circuit treatments.

SCAN hyperconnectivity as a PD biomarker

Previous studies have reported RSFC hyperconnectivity between subcortical regions and what was at the time believed to be the M1

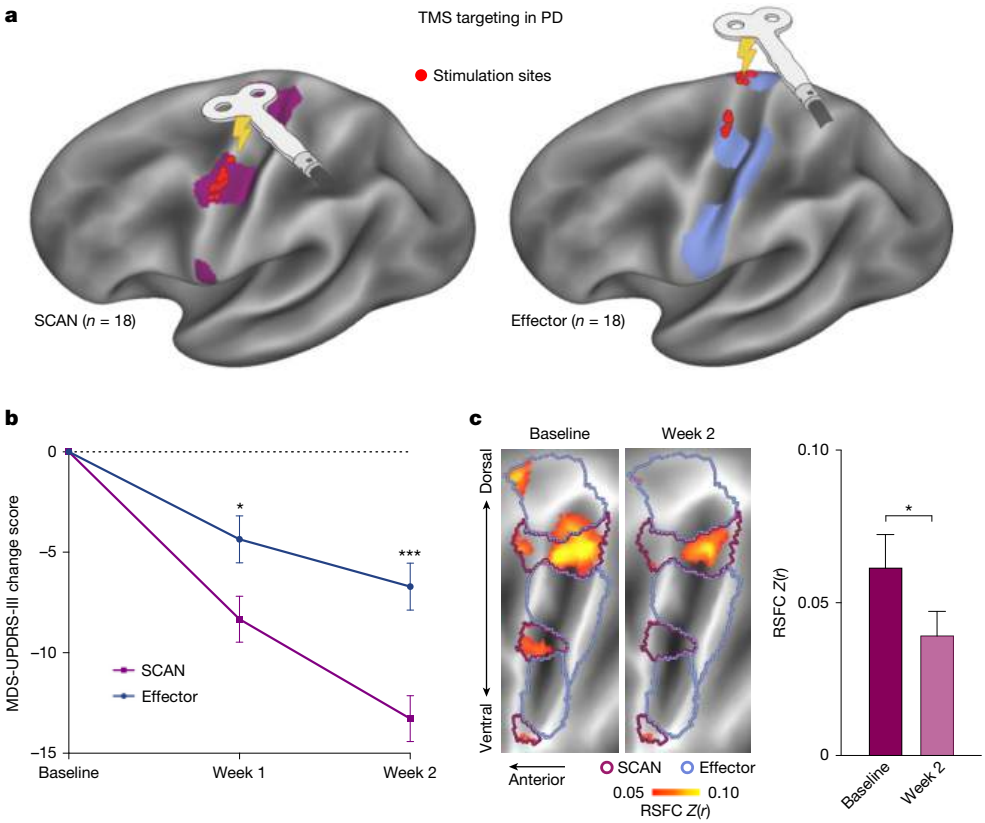

Fig. 5 | TMS targeting the SCAN versus effector-specific motor regions. **a**, In total, 36 patients with PDwere randomly assigned to receive iTBS either over personalized SCAN or effector-specific motor regions. Each patient's functional networks in the M1 along the central sulcus were mapped using prestimulation RSFC data (Methods and Supplementary Fig. 13a). Personalized targets were mapped and displayed on a standard cortical surface template (left hemisphere), with each red dot representing a target for a patient. Each patient received accelerated iTBS (7,200 pulses per day) for 14 consecutive days (Methods and Supplementary Fig. 13b). **b**, Clinical improvements in PD. The SCAN group ($n = 18$) showed a significantly larger reduction in overall motor symptoms, measured by the MDS-UPDRS-III total score, compared with the effector group ($n = 17$; LME model: 1-week mean difference (MD) = −3.98, Bonferroni corrected $P = 0.0350$; 2-week MD = −6.57, Bonferroni corrected $P = 0.0003$). They also experienced faster symptom relief (LME model, group-by-time interaction, $P = 0.0002$). The black asterisk indicates comparisons of MDS-UPDRS-III score changes between the two groups at week 1 or week 2. Data are mean ± s.e.m. **c**, Functional connectivity after SCAN TMS. Group-averaged cortical functional connectivity maps seeded from subcortical regions are shown on flattened M1 surfaces, with stronger connectivity with the SCAN (purple outlines) than with effector-specific regions (blue outlines) (left). The cortico–subcortical SCAN hyperconnectivity at the baseline decreased after the 2-week stimulation ($n = 14$). Right, SCAN stimulation significantly reduced the hyperconnectivity between subcortical regions and the SCAN (week 2 versus baseline: one-tailed paired t-test, $^*P = 0.039$). Data are mean ± s.e.m.

(refs. 57–59). Here, analyses of independent datasets revealed robust cortico–subcortical RSFC hyperconnectivity specifically within the SCAN in PD. RSFC among presumed motor regions in the central sulcus has been linked to beta-band coherence that reflects the synchronization of neural activity between brain regions within the beta frequency range (typically 13–35 Hz)[60–62]. This coherence is crucial for motor planning and aligns with the SCAN's functions[63,64]. The RSFC hyperconnectivity in PD coincides with increased beta-band synchronization between the precentral gyrus/central sulcus and globus pallidus/STN, which has been observed in both human and animal studies of PD[24,65–69]. This enhanced synchronization probably results from phase-locked action-potential firing within the motor cortex–basal ganglia circuit[65]. Elucidating the direct relationship between these measures requires future investigations in which fMRI and electrophysiological recordings are obtained within the same individuals.

Dopaminergic medications and neuromodulation have been shown to suppress cortico–subcortical beta-band hypersynchronization[24,68,70–72]. We have now shown that SCAN cortico–subcortical RSFC hyperconnectivity is specifically downregulated by dopaminergic medications and various neuromodulation treatments in patients with PD. Moreover, SCAN hyperconnectivity was specific to PD and absent in the other three movement disorders. Thus, SCAN RSFC hyperconnectivity may serve as a non-invasive biomarker for PD[73], in addition to electrophysiology-based beta-band synchronization biomarkers[73,74] and other imaging-based biomarkers[75], such as the PDRP[20,22,23]. It is worth investigating its use in differential diagnosis, monitoring disease progression, guiding personalized therapeutic strategies and objectively assessing treatment outcomes in future studies[76–81]. Despite the challenges posed by the limited signal-to-noise ratio of fMRI in deep brain nuclei, advances in imaging sequences[82–84], ultra-high field MRI[85–87] and optimized processing methods[88–92] will further enhance the feasibility of this approach.

SCAN provides new PD treatment targets

Neuromodulation techniques offer considerable benefits to patients with PD, particularly in improving symptoms and managing motor fluctuations[26,93]. Among these techniques, DBS so far has been the most successful. However, only a small proportion (less than 10%) of patients with PD are suitable DBS candidates[94]. Such issues highlight the need for a comprehensive toolkit that spans subcortical and cortical surface SCAN targets, incorporating both invasive and non-invasive methods, such as DBS, low- and high-intensity focused ultrasound, TMS and electrical cortical stimulation[25,38,95,96] (Extended Data Fig. 10). Such a toolkit would enable physicians to tailor treatment to the specific needs of each patient at different stages of their disease.

For established therapeutics targeting deep subcortical nuclei for PD, identifying the SCAN representation in these nuclei based on RSFC may optimize target localization and further improve clinical benefits. As shown by our focused ultrasound study, a functionally defined thalamic SCAN node might be the optimal target. Similarly, the optimal stimulation sites of DBS converge onto the SCAN circuit. Thus, incorporating personalized SCAN RSFC with other advanced imaging modalities[29,77] may assist target localization for DBS[51].

Besides deep brain targets, surface SCAN targets on the cerebral cortex show great potential as alternatives for PD treatment. In our study, targeting personalized cortical SCAN nodes with rTMS significantly accelerated symptom alleviation and doubled the clinical efficacy without adverse effects, compared with targeting the effector-specific regions, highlighting the importance of precise target localization. Implanted epidural/subdural electrode strips targeting the cortical SCAN nodes may also have critical roles, either by recording control signals or delivering direct cortical stimulation[28,97]. Contacts that provided robust cortical control signals for closed-loop aDBS, which improved clinical efficacy while minimizing adverse effects, were more proximal to SCAN than to effector regions (Extended Data Fig. 7). Intraoperative direct cortical stimulation or implanted epidural stimulators in the precentral gyrus have also shown clinical efficacy with transient disappearance of severe parkinsonism in some cases[98] or long-lasting improvements in motor symptoms in some studies[97]. Although the exact stimulation sites of these studies are yet to be determined, we speculate that stimulating the SCAN rather than other effector-specific nodes will yield more beneficial outcomes in PD, as demonstrated by our rTMS study. Thus, one can conceive of a new implantation procedure of epidural/subdural electrodes that uses personalized SCAN mapping for target selection and uses rTMS to validate clinical responses before implantation. It is worth testing whether such an approach would involve a simpler surgical procedure compared with targeting subcortical nuclei, with less invasiveness, while offering the potential for long-term control of motor symptoms akin to DBS. It would also be valuable to explore whether dual-site stimulation, combining the subcortical and cortical SCAN stimulation, could provide further benefits compared with DBS. Moreover, stimulating different SCAN nodes, which show modestly different RSFC patterns (see extended data figure 5 of ref. 6) may correspond to effects on distinct symptoms, potentially enabling more-refined treatment strategies for specific symptom domains[29].

PD as a somato-cognitive action disorder

PD has traditionally been classified as a movement disorder on the basis of its most visible and debilitating symptoms, despite the well-recognized complex deficits in movement planning, coordination and cognitive abilities. Here we provide evidence that the SCAN lies at the core of network dysfunction in PD. With this updated understanding, we propose that PD may be better conceptualized and treated as a SCAN disorder. While SCAN dysfunction is not exclusive to a single condition—as it could also arise from stroke or multiple sclerosis—our findings position PD as a paradigmatic instance of a SCAN disorder. This reclassification of PD shifts the focus from complex and diverse phenotypic symptoms to specific circuit pathologies, encouraging future research on the associations between network dysfunction and the various symptom domains of PD. Highlighting the SCAN dysfunction in PD should facilitate the optimization of existing therapies and the development of circuit-based neuromodulation treatments.

Online content

Any methods, additional references, Nature Portfolio reporting summaries, source data, extended data, supplementary information, acknowledgements, peer review information; details of author contributions and competing interests; and statements of data and code availability are available at https://doi.org/10.1038/s41586-025-10059-1.

1. Bloem, B. R., Okun, M. S. & Klein, C. Parkinson's disease. *Lancet* **397**, 2284–2303 (2021).
2. Armstrong, M. J. & Okun, M. S. Diagnosis and treatment of Parkinson disease. *JAMA* **323**, 548–560 (2020).
3. McGregor, M. M. & Nelson, A. B. Circuit mechanisms of Parkinson's disease. *Neuron* **101**, 1042–1056 (2019).
4. Sveinbjornsdottir, S. The clinical symptoms of Parkinson's disease. *J. Neurochem.* **139**, 318–324 (2016).
5. Blesa, J., Foffani, G., Dehay, B., Bezard, E. & Obeso, J. A. Motor and non-motor circuit disturbances in early Parkinson disease: which happens first? *Nat. Rev. Neurosci.* **23**, 115–128 (2022).
6. Gordon, E. M. et al. A somato-cognitive action network alternates with effector regions in motor cortex. *Nature* **617**, 351–359 (2023).
7. Jensen, M. A. et al. A motor association area in the depths of the central sulcus. *Nat. Neurosci.* **26**, 1165–1169 (2023).
8. Mirelman, A. et al. Gait impairments in Parkinson's disease. *Lancet Neurol.* **18**, 697–708 (2019).
9. Bakker, M. et al. Effects of stereotactic neurosurgery on postural instability and gait in Parkinson's disease. *Mov. Disord.* **19**, 1092–1099 (2004).
10. Lau, B. et al. Axial symptoms predict mortality in patients with Parkinson disease and subthalamic stimulation. *Neurology* **92**, e2559–e2570 (2019).
11. Benecke, R., Rothwell, J., Dick, J., Day, B. & Marsden, C. Performance of simultaneous movements in patients with Parkinson's disease. *Brain* **109**, 739–757 (1986).
12. Schwab, R. S., Chafetz, M. E. & Walker, S. Control of two simultaneous voluntary motor acts in normals and in parkinsonism. *AMA Arch. Neurol. Psychiatry* **72**, 591–598 (1954).
13. Chaudhuri, K. R., Healy, D. G. & Schapira, A. H. Non-motor symptoms of Parkinson's disease: diagnosis and management. *Lancet Neurol.* **5**, 235–245 (2006).
14. Marsden, C. Slowness of movement in Parkinson's disease. *Mov. Disord.* **4**, S26–S37 (1989).
15. Nutt, J. G. et al. Freezing of gait: moving forward on a mysterious clinical phenomenon. *Lancet Neurol.* **10**, 734–744 (2011).
16. Helmich, R. C. et al. Cognitive load amplifies Parkinson's tremor through excitatory network influences onto the thalamus. *Brain* **143**, 1498–1511 (2020).
17. Bonanni, L., Thomas, A. & Onofrj, M. Paradoxical kinesia in parkinsonian patients surviving earthquake. *Mov. Disord.* **25**, 1302–1304 (2010).
18. Poewe, W. et al. Parkinson disease. *Nat. Rev. Dis. Primers* **3**, 17013 (2017).
19. DeLong, M. R. & Wichmann, T. Basal ganglia circuits as targets for neuromodulation in Parkinson disease. *JAMA Neurol.* **72**, 1354–1360 (2015).
20. Eckert, T., Tang, C. & Eidelberg, D. Assessment of the progression of Parkinson's disease: a metabolic network approach. *Lancet Neurol.* **6**, 926–932 (2007).
21. Ji, G.-J. et al. Functional connectivity of the corticobasal ganglia–thalamocortical network in Parkinson disease: a systematic review and meta-analysis with cross-validation. *Radiology* **287**, 973–982 (2018).
22. Schindlbeck, K. A. & Eidelberg, D. Network imaging biomarkers: insights and clinical applications in Parkinson's disease. *Lancet Neurol.* **17**, 629–640 (2018).
23. Perovnik, M., Rus, T., Schindlbeck, K. A. & Eidelberg, D. Functional brain networks in the evaluation of patients with neurodegenerative disorders. *Nat. Rev. Neurol.* **19**, 73–90 (2022).
24. Binns, T. S. et al. Shared pathway-specific network mechanisms of dopamine and deep brain stimulation for the treatment of Parkinson's disease. *Nat. Commun.* **16**, 3587 (2025).
25. Goede, L. L. et al. Linking invasive and noninvasive brain stimulation in Parkinson's disease: a randomized trial. *Mov. Disord.* **39**, 1971–1981 (2024).
26. Okun, M. S. Deep-brain stimulation for Parkinson's disease. *N. Engl. J. Med.* **367**, 1529–1538 (2012).
27. Miocinovic, S., Somayajula, S., Chitnis, S. & Vitek, J. L. History, applications, and mechanisms of deep brain stimulation. *JAMA Neurol.* **70**, 163–171 (2013).
28. Oehrn, C. R. et al. Chronic adaptive deep brain stimulation versus conventional stimulation in Parkinson's disease: a blinded randomized feasibility trial. *Nat. Med.* **30**, 3345–3356 (2024).
29. Rajamani, N. et al. Deep brain stimulation of symptom-specific networks in Parkinson's disease. *Nat. Commun.* **15**, 4662 (2024).
30. Ferraye, M. U., Debû, B. & Pollak, P. Deep brain stimulation effect on freezing of gait. *Mov. Disord.* **23**, S489–S494 (2008).
31. Zhang, W. et al. Efficacy of repetitive transcranial magnetic stimulation in Parkinson's disease: a systematic review and meta-analysis of randomised controlled trials. *EClinicalMedicine* **52**, 101589 (2022).
32. Dum, R. P., Levinthal, D. J. & Strick, P. L. The mind-body problem: circuits that link the cerebral cortex to the adrenal medulla. *Proc. Natl Acad. Sci. USA* **116**, 26321–26328 (2019).
33. Levinthal, D. J. & Strick, P. L. Multiple areas of the cerebral cortex influence the stomach. *Proc. Natl Acad. Sci. USA* **117**, 13078–13083 (2020).
34. Graziano, M. S. A. Fundamental principles of cortical organization reflected in a new study. *Neuron* **111**, 1524–1525 (2023).
35. Graziano, M. S. A. Ethological action maps: a paradigm shift for the motor cortex. *Trends Cogn. Sci.* **20**, 121–132 (2016).
36. Dosenbach, N. U. F., Raichle, M. E. & Gordon, E. M. The brain's action-mode network. *Nat. Rev. Neurosci.* **26**, 158–168 (2025).
37. Seeley, W. W., Crawford, R. K., Zhou, J., Miller, B. L. & Greicius, M. D. Neurodegenerative diseases target large-scale human brain networks. *Neuron* **62**, 42–52 (2009).
38. Fox, M. D. et al. Resting-state networks link invasive and noninvasive brain stimulation across diverse psychiatric and neurological diseases. *Proc. Natl Acad. Sci. USA* **111**, E4367–E4375 (2014).
39. Elias, G. J. B. et al. Probabilistic mapping of deep brain stimulation: insights from 15 years of therapy. *Ann. Neurol.* **89**, 426–443 (2021).

40. Lynch, C. J. et al. Frontostriatal salience network expansion in individuals in depression. *Nature* **633**, 624–633 (2024).
41. Siegel, J. S. et al. Psilocybin desynchronizes the human brain. *Nature* **632**, 131–138 (2024).
42. Gordon, E. M. et al. Precision functional mapping of individual human brains. *Neuron* **95**, 791–807 (2017).
43. Dworetsky, A. et al. Two common and distinct forms of variation in human functional brain networks. *Nat. Neurosci.* **27**, 1187–1198 (2024).
44. Jacobs, E. G. Leveraging precision neuroimaging to advance women's brain health. *Nat. Mental Health* **1**, 700–701 (2023).
45. Laumann, T. O. et al. Functional system and areal organization of a highly sampled individual human brain. *Neuron* **87**, 657–670 (2015).
46. Poldrack, R. A. et al. Long-term neural and physiological phenotyping of a single human. *Nat. Commun.* **6**, 8885 (2015).
47. Pritschet, L. et al. Neuroanatomical changes observed over the course of a human pregnancy. *Nat. Neurosci.* **27**, 2253–2260 (2024).
48. Jorge, A. et al. Hyperdirect connectivity of opercular speech network to the subthalamic nucleus. *Cell Rep.* **38**, 110477 (2022).
49. Dahmani, L. et al. Focused ultrasound thalamotomy for tremor treatment impacts the cerebello-thalamo-cortical network. *NPJ Parkinsons Dis.* **9**, 90 (2023).
50. Meng, Y., Hynynen, K. & Lipsman, N. Applications of focused ultrasound in the brain: from thermoablation to drug delivery. *Nat. Rev. Neurol.* **17**, 7–22 (2020).
51. Greene, D. J. et al. Integrative and network-specific connectivity of the basal ganglia and thalamus defined in individuals. *Neuron* **105**, 742–758 (2020).
52. Dudman, J. T. & Krakauer, J. W. The basal ganglia: from motor commands to the control of vigor. *Curr. Opin. Neurobiol.* **37**, 158–166 (2016).
53. Wager, T. D. et al. An fMRI-based neurologic signature of physical pain. *N. Engl. J. Med.* **368**, 1388–1397 (2013).
54. Woo, C.-W. et al. Separate neural representations for physical pain and social rejection. *Nat. Commun.* **5**, 5380 (2014).
55. Desmurget, M. et al. Neural representations of ethologically relevant hand/mouth synergies in the human precentral gyrus. *Proc. Natl Acad. Sci. USA* **111**, 5718–5722 (2014).
56. Desmurget, M. & Sirigu, A. Revealing humans' sensorimotor functions with electrical cortical stimulation. *Philos. Trans. R. Soc. B* **370**, 20140207 (2015).
57. Baudrexel, S. et al. Resting state fMRI reveals increased subthalamic nucleus-motor cortex connectivity in Parkinson's disease. *Neuroimage* **55**, 1728–1738 (2011).
58. Hacker, C. D., Perlmutter, J. S., Criswell, S. R., Ances, B. M. & Snyder, A. Z. Resting state functional connectivity of the striatum in Parkinson's disease. *Brain* **135**, 3699–3711 (2012).
59. Kurani, A. S. et al. Subthalamic nucleus–sensorimotor cortex functional connectivity in de novo and moderate Parkinson's disease. *Neurobiol. Aging* **36**, 462–469 (2015).
60. Mantini, D., Perrucci, M. G., Del Gratta, C., Romani, G. L. & Corbetta, M. Electrophysiological signatures of resting state networks in the human brain. *Proc. Natl Acad. Sci. USA* **104**, 13170–13175 (2007).
61. Brookes, M. J. et al. Measuring functional connectivity using MEG: methodology and comparison with fcMRI. *Neuroimage* **56**, 1082–1104 (2011).
62. Weinrich, C. A. et al. Modulation of long-range connectivity patterns via frequency-specific stimulation of human cortex. *Curr. Biol.* **27**, 3061–3068 (2017).
63. Khanna, P. & Carmena, J. M. Neural oscillations: beta band activity across motor networks. *Curr. Opin. Neurobiol.* **32**, 60–67 (2015).
64. Little, S., Bonaiuto, J., Barnes, G. & Bestmann, S. Human motor cortical beta bursts relate to movement planning and response errors. *PLoS Biol.* **17**, e3000479 (2019).
65. Cagnan, H. et al. Temporal evolution of beta bursts in the parkinsonian cortical and basal ganglia network. *Proc. Natl Acad. Sci. USA* **116**, 16095–16104 (2019).
66. Wang, D. D. et al. Pallidal deep-brain stimulation disrupts pallidal beta oscillations and coherence with primary motor cortex in Parkinson's disease. *J. Neurosci.* **38**, 4556–4568 (2018).
67. Hirschmann, J. et al. Distinct oscillatory STN-cortical loops revealed by simultaneous MEG and local field potential recordings in patients with Parkinson's disease. *Neuroimage* **55**, 1159–1168 (2011).
68. Eusebio, A. et al. Resonance in subthalamo-cortical circuits in Parkinson's disease. *Brain* **132**, 2139–2150 (2009).
69. Guerra, A. et al. Enhancing gamma oscillations restores primary motor cortex plasticity in Parkinson's disease. *J. Neurosci.* **40**, 4788–4796 (2020).
70. Oswal, A. et al. Deep brain stimulation modulates synchrony within spatially and spectrally distinct resting state networks in Parkinson's disease. *Brain* **139**, 1482–1496 (2016).
71. Kato, K. et al. Bilateral coherence between motor cortices and subthalamic nuclei in patients with Parkinson's disease. *Clin. Neurophysiol.* **126**, 1941–1950 (2015).
72. Torrecillos, F., He, S., Kühn, A. A. & Tan, H. Average power and burst analysis revealed complementary information on drug-related changes of motor performance in Parkinson's disease. *NPJ Parkinsons Dis.* **9**, 93 (2023).
73. Woo, C.-W., Chang, L. J., Lindquist, M. A. & Wager, T. D. Building better biomarkers: brain models in translational neuroimaging. *Nat. Neurosci.* **20**, 365–377 (2017).
74. Bouthour, W. et al. Biomarkers for closed-loop deep brain stimulation in Parkinson disease and beyond. *Nat. Rev. Neurol.* **15**, 343–352 (2019).
75. Zarkali, A., Thomas, G. E. C., Zetterberg, H. & Weil, R. S. Neuroimaging and fluid biomarkers in Parkinson's disease in an era of targeted interventions. *Nat. Commun.* **15**, 5661 (2024).
76. Hirschmann, J., Steina, A., Vesper, J., Florin, E. & Schnitzler, A. Neuronal oscillations predict deep brain stimulation outcome in Parkinson's disease. *Brain Stimul.* **15**, 792–802 (2022).
77. Horn, A. et al. Connectivity predicts deep brain stimulation outcome in Parkinson disease. *Ann. Neurol.* **82**, 67–78 (2017).
78. Neumann, W. J., Gilron, R., Little, S. & Tinkhauser, G. Adaptive deep brain stimulation: from experimental evidence toward practical implementation. *Mov. Disord.* **38**, 937–948 (2023).
79. Alagapan, S. et al. Cingulate dynamics track depression recovery with deep brain stimulation. *Nature* **622**, 130–138 (2023).
80. He, S. et al. Beta-triggered adaptive deep brain stimulation during reaching movement in Parkinson's disease. *Brain* **146**, 5015–5030 (2023).
81. Vaillancourt, D. E. et al. Automated imaging differentiation for parkinsonism. *JAMA Neurol.* **82**, 495–505 (2025).
82. Lynch, C. J. et al. Rapid precision functional mapping of individuals using multi-echo fMRI. *Cell Rep.* **33**, 108540 (2020).
83. Kundu, P. et al. Multi-echo fMRI: a review of applications in fMRI denoising and analysis of BOLD signals. *Neuroimage* **154**, 59–80 (2017).
84. Yang, Z. & Lewis, L. D. Imaging the temporal dynamics of brain states with highly sampled fMRI. *Curr. Opin. Behav. Sci.* **40**, 87–95 (2021).
85. Plantinga, B. R. et al. Individualized parcellation of the subthalamic nucleus in patients with Parkinson's disease with 7T MRI. *Neuroimage* **168**, 403–411 (2018).
86. Huber, L. et al. Sub-millimeter fMRI reveals multiple topographical digit representations that form action maps in human motor cortex. *Neuroimage* **208**, 116463 (2020).
87. Lewis, L. D., Setsompop, K., Rosen, B. R. & Polimeni, J. R. Stimulus-dependent hemodynamic response timing across the human subcortical-cortical visual pathway identified through high spatiotemporal resolution 7T fMRI. *Neuroimage* **181**, 279–291 (2018).
88. Ciric, R. et al. Mitigating head motion artifact in functional connectivity MRI. *Nat. Protoc.* **13**, 2801–2826 (2018).
89. Yan, Y. et al. Reconstructing lost BOLD signal in individual participants using deep machine learning. *Nat. Commun.* **11**, 5046 (2020).
90. Ren, J. et al. SUGAR: spherical ultrafast graph attention framework for cortical surface registration. *Med. Image Anal.* **94**, 103122 (2024).
91. Ren, J. et al. Fast cortical surface reconstruction from MRI using deep learning. *Brain Inform.* **9**, 6 (2022).
92. Ren, J. et al. DeepPrep: an accelerated, scalable and robust pipeline for neuroimaging preprocessing empowered by deep learning. *Nat. Methods* **22**, 473–476 (2025).
93. Okun, M. S. et al. Subthalamic deep brain stimulation with a constant-current device in Parkinson's disease: an open-label randomised controlled trial. *Lancet Neurol.* **11**, 140–149 (2012).
94. Morgante, L. et al. How many parkinsonian patients are suitable candidates for deep brain stimulation of subthalamic nucleus? Results of a questionnaire. *Parkinsonism Relat. Disord.* **13**, 528–531 (2007).
95. Siddiqi, S. H. et al. Brain stimulation and brain lesions converge on common causal circuits in neuropsychiatric disease. *Nat. Hum. Behav.* **5**, 1707–1716 (2021).
96. Riis, T. S., Feldman, D. A., Losser, A. J., Okifuji, A. & Kubanek, J. Noninvasive targeted modulation of pain circuits with focused ultrasonic waves. *Pain* **165**, 2829–2839 (2024).
97. Lavano, A. et al. Minimally invasive motor cortex stimulation for Parkinson's disease. *J. Neurosurg. Sci.* **61**, 77–87 (2016).
98. Woolsey, C. N., Erickson, T. C. & Gilson, W. E. Localization in somatic sensory and motor areas of human cerebral cortex as determined by direct recording of evoked potentials and electrical stimulation. *J. Neurosurg.* **51**, 476–506 (1979).

[1]Changping Laboratory, Beijing, China. [2]Academy for Advanced Interdisciplinary Studies, Peking University, Beijing, China. [3]Athinoula A. Martinos Center for Biomedical Imaging, Department of Radiology, Massachusetts General Hospital, Charlestown, MA, USA. [4]Harvard Medical School, Boston, MA, USA. [5]Mallinckrodt Institute of Radiology, Washington University School of Medicine, St Louis, MO, USA. [6]Allied Labs for Imaging Guided Neurotherapies (ALIGN), Washington University School of Medicine, St Louis, MO, USA. [7]College of Future Technology, Peking University, Beijing, China. [8]State Key Laboratory of Cognitive Neuroscience and Learning, Beijing Normal University, Beijing, China. [9]National Engineering Research Center of Neuromodulation, School of Aerospace Engineering, Tsinghua University, Beijing, China. [10]Department of Medical Imaging, Henan Provincial People's Hospital & People Hospital of Zhengzhou University, Zhengzhou, China. [11]Department of Neurosurgery, Massachusetts General Hospital, Boston, MA, USA. [12]Department of Neurology, Peking University First Hospital, Beijing, China. [13]Department of Neurological Surgery, University of California, San Francisco, San Francisco, CA, USA. [14]Department of Radiology and Biomedical Imaging, University of California, San Francisco, CA, USA. [15]Weill Institute for Neurosciences, University of California, San Francisco, San Francisco, CA, USA. [16]Clinical Neuroscience Center, Ruijin Hospital Luwan Branch, Shanghai Jiaotong University School of Medicine, Shanghai, China. [17]Department of Neurology, Neurosurgery, Psychiatry and Neuroscience,

Ruijin Hospital Shanghai Jiaotong University School of Medicine, Shanghai, China. [18]School of Mental Health and Psychological Sciences, Anhui Medical University, Hefei, China. [19]Department of Neurology, The First Affiliated Hospital of Anhui Medical University, Anhui Medical University, Hefei, China. [20]Anhui Province Key Laboratory of Cognition and Neuropsychiatric Disorders, Hefei, China. [21]Department of Neurology, Peking University Third Hospital, Beijing, China. [22]Department of Physical Therapy, MGH Institute of Health Professions, Boston, MA, USA. [23]Department of Rehabilitation Science, MGH Institute of Health Professions, Boston, MA, USA. [24]Department of Neurology, University of California, San Francisco, San Francisco, CA, USA. [25]Graduate Program in Bioengineering, University of California, Berkeley and University of California, San Francisco, San Francisco, CA, USA. [26]IDG/McGovern Institute for Brain Research at Tsinghua University, Beijing, China. [27]State Key Laboratory of Metabolic Dysregulation & Prevention and Treatment of Esophageal Cancer, Zhengzhou University, Zhengzhou, China. [28]Department of Neurology, Washington University School of Medicine, St Louis, MO, USA. [29]Department of Biomedical Engineering, Washington University in St Louis, St Louis, MO, USA. [30]Department of Psychological and Brain Sciences, Washington University in St Louis, St Louis, MO, USA. [31]Department of Pediatrics, Washington University School of Medicine, St Louis, MO, USA. [32]Biomedical Pioneering Innovation Center, Peking University, Beijing, China. [33]These authors contributed equally: Jianxun Ren, Wei Zhang. ✉e-mail: jianxun.ren@cpl.ac.cn; mywang@ha.edu.cn; wangdanhong@cpl.ac.cn; hesheng@biopic.pku.edu.cn

Methods

Participants

In this study, we used 11 independent datasets comprising 863 total participants after quality control. These datasets include (1) PIPD dataset[99]: 166 patients with PD and 60 HC individuals; (2) DBS-fMRI dataset: 14 patients with PD, with evaluations conducted both before and after DBS surgery, along with 25 HC individuals; (3) TMS dataset: 36 patients with PD; (4) DBS-SS dataset: 342 patients with PD; (5) DBS-ECoG dataset: 17 patients with PD who underwent STN-DBS surgery and DBS-evoked ECoG recording; (6) MRgFUS dataset: 10 patients with tremor-dominant PD; (7) aDBS dataset: 4 patients with PD; (8) LCT dataset: 21 patients with PD; (9) ET dataset[100]: 45 patients with ET and 45 HC individuals from the PIPD dataset; (10) dystonia dataset: 42 patients with dystonia and 21 HC individuals; and (11) ALS dataset: 30 patients with ALS and 30 HC individuals. PD was diagnosed according to the revised clinical diagnostic criteria of the International Movement Disorder Society (MDS, 2015 version) or the Chinese Parkinson's Disease Diagnostic Criteria (2016 version). The following sections provide detailed descriptions for each dataset.

PIPD dataset

Patients. In total, 180 patients with PD were recruited from Henan Provincial People's Hospital (HPPH), China. The inclusion criteria included being aged 18 years or above and a clinical diagnosis of PD. Exclusion criteria comprised the following: (1) MRI contraindications; (2) a history of neurological disorders aside from PD, including stroke, cerebrovascular disease, seizures and brain tumours; (3) previous invasive neurosurgeries such as DBS or ablation; and (4) average relative head motion larger than 0.2 mm during rsfMRI scanning. Four patients did not complete MRI scanning, and ten patients were excluded owing to excessive head motion. Ultimately, 166 patients were included in the analysis (64 women, 102 men; mean ± s.d. age = 61.8 ± 7.84 years; demographic and clinical details are provided in Extended Data Table 1).

HC participants. In total, 71 healthy participants aged 18 years or older, lacking neurological or psychiatric disorders, were enrolled. Exclusion criteria included MRI contraindications and an average relative head motion exceeding 0.2 mm. After excluding 11 participants owing to excessive head motion, the analysis included 60 HC participants (34 women, 26 men; mean ± s.d. age = 56.10 ± 6.64 years; Extended Data Table 1). The control group exhibited significantly different demographics from the PD group. We therefore sampled a subset of 65 patients with PD from the 166 patients to ensure demographic matching when performing case–control analyses (Extended Data Table 1). The experimental protocol was approved by the HPPH Institutional Review Board (IRB). Written informed consent was obtained from all of the participants.

MRI acquisition. The participants underwent one structural MRI scan lasting 8 min and 50 s, and five scans, each spanning 6 min and 14 s, resulting in a cumulative scan duration of 31 min and 10 s. MRI was performed using the Siemens 3 T Prisma MRI scanner equipped with a 64-channel head coil. The structural scans involved T1-weighted images acquired through a MP2RAGE sequence (TI1 = 755 ms, TI2 = 2500 ms, TE = 3.43 ms, TR = 5,000 ms, flip angle1 = 4°, flip angle2 = 5°, matrix size = 256 × 256, 208 sagittal slices, spatial resolution = 1 × 1 × 1 mm^3). An acceleration factor of 3 (with 32 reference lines) was applied in the primary phase encoding direction, with online GRAPPA image reconstruction. rsfMRI data were acquired using a gradient-echo echo planar imaging (GE-EPI) sequence (TE = 35 ms, TR = 2,000 ms, flip angle = 80°, and 75 slices, spatial resolution = 2.2 × 2.2 × 2.2 mm^3). During data acquisition, the participants were instructed to keep their eyes open, remain awake while keeping their body still and minimize head movement.

DBS-fMRI dataset

Patients. This dataset is a part of the 3 T MRI-compatible DBS cohort. A total of 14 patients (5 women, 9 men; mean ± s.d. age = 54.71 ± 7.65 years) diagnosed with the akinetic-rigid dominant form of clinically diagnosed PD were recruited from three centres, including Tiantan Hospital, Beijing; Peking Union Medical College Hospital, Beijing; and Qilu Hospital, Jinan, China. Ethics approval for this project was granted by the ethics committees of Tiantan Hospital (QX2016-009-02, 21 July 2016), Peking Union Medical College Hospital (HS2016094, 21 September 2016) and Qilu Hospital (2016008, 28 August 2016), with ClinicalTrails.gov identifier NCT02937727. Written informed consent was obtained from all of the participating individuals. Inclusion criteria consisted of: (1) aged between 18 and 75 years; (2) MMSE score above 24; (3) Hoehn–Yahr scale above stage two in the medication off status; (4) PD duration exceeding 5 years; (5) established positive response to dopaminergic medication (at least 30% UPDRS-III improvement with levodopa); and (6) ability to provide informed consent, assessed through preoperative neuropsychological evaluation. Exclusion criteria encompassed: (1) ineligibility for DBS, such as anaesthesia complications; (2) history of hydrocephalus, brain atrophy, cerebral infarction or cerebrovascular diseases; (3) inability to comply with verbal instructions; (4) the presence of severe pathological chronic conditions that might confound treatment effect or data interpretation; (e) MRI contraindications or inability to complete MRI scans. Out of the initial cohort, 11 patients had a complete dataset, whereas three patients had incomplete data due to missing post-surgical visits (DBS01 after the 1-month follow-up, DBS03 after the 3-month follow-up, and DBS08 at the 1-month follow-up only).

Each patient underwent standard frame-based stereotaxic DBS implantation surgery at one of the aforementioned medical institutions. The bilateral STNs were the targeted regions for DBS, localized through presurgical structural MRI scans, intraoperative electrophysiological recordings and observed motor symptom improvement during the surgery. Two quadripolar DBS electrodes (Model L301C, Pins Medical) were bilaterally implanted into the STN for each patient. A low-field-potential sensing-enabled neurostimulator (G106R, Beijing Pins Medical) was connected to the leads (Model E202C, Pins Medical) during a single operation. The DBS stimulator and electrodes were compatible with the 3 T MRI environment and proven safe for MRI scans with implantation. At each post-surgical visit, a team of two neurologists managed each patient's DBS system. Optimized DBS programming, resulting in optimal motor symptom improvement, was achieved by selecting positive and negative contacts and determining stimulation frequency, amplitude and pulse width.

HC participants. HC participants matched in age to the patient group were recruited. Similar exclusion criteria were applied, encompassing relevant medical history, ability to follow instructions, conditions that could complicate data interpretation, MRI contraindications and average relative head motion exceeding 0.2 mm. The control group comprised 28 participants. One participant was excluded owing to incomplete MRI data caused by discomfort in the scanner, and two participants were excluded owing to excessive head motion, leaving 25 participants suitable for the case–control analysis (Extended Data Table 1; 13 women and 12 men; mean ± s.d. age = 56.32 ± 6.88 years).

MRI acquisition. The participants underwent data acquisition across five visits—one presurgical and four post-surgical follow-up visits. The presurgical visit occurred approximately 1 month before the DBS surgery, whereas the post-surgical visits occurred at 1, 3, 6 and 12 months after surgery. MRI scans, neurological assessments and computerized tomography (CT) scans were performed. Notably, the presurgical

visit involved one T1w MRI run and five rsfMRI runs (totalling 31 min of rsfMRI). For each post-surgical visit, the participants underwent four runs of DBS ON (130 Hz continuous stimulation) blood-oxygen-level-dependent (BOLD) fMRI (25 min) followed by four runs of DBS OFF fMRI (25 min). The control participants had one visit, involving one T1-weighted MRI run and three BOLD fMRI runs lasting 19 min in total.

All MRI data were collected using the 3 T Philips Achieva TX whole-body MRI scanner equipped with a 32-channel head coil. T1-weighted structural images were acquired using a MPRAGE sequence, lasting 4 min and 14 s (TE = 3.70 ms, TR = 7.52 ms, flip angle = 8°, 180 sagittal slices, spatial resolution = $1 \times 1 \times 1\ mm^3$). Functional images were acquired with a 6-min and 14-s transversal GE-EPI sequence (TE = 30 ms, TR = 2,000 ms, flip angle = 90°, 37 slices, spatial resolution = $2.875 \times 2.875 \times 4\ mm^3$, 184 frames per run). CT images were acquired using the uCT 760 (United Imaging) scanner 1 month after surgery. A head helical sequence, with FOV = 512 × 512, pixel spacing = 0.449 mm × 0.449 mm, 204 slices, slice thickness = 0.625 mm, was used.

TMS dataset

Patients. The participants were recruited at HPPH from 29 May 2023 to 28 April 2024. The study protocol was approved by the institutional ethics committee of HPPH (2023LS37, 7 May 2023). Written informed consent was obtained from all of the participating individuals. Registration of this study was not required according to ClinicalTrials.gov. However, the study was registered to ensure transparency, with the ClinicalTrials.gov identifier NCT06734676. Inclusion criteria included: (1) confirmed diagnosis of PD; (2) age 18 to 75 years; (3) stable anti-PD medication treatment for a minimum of 2 months; (4) MMSE score above 24; and (5) providing signed informed consent. Exclusion criteria included: (1) confirmed diagnosis of other neurological disorders; (2) implanted medical devices; (3) contraindications to MRI scanning and TMS; (4) personal or family history of epilepsy; (5) previous neuromodulation treatments within the past 3 months; (6) other health abnormalities that the investigator deems unsuitable for study participation.

In the study, 36 patients with PD (13 women, 23 men; mean age = 65.06 ± 6.82 years; Extended Data Table 1) were randomly divided into two groups at a ratio of 1:1, where one group received SCAN stimulation (SCAN group, $n = 18$) and the other M1 effector-specific stimulation (effector group, $n = 18$), over a span of 14 consecutive days. The randomization codes were generated using a custom script by an independent research assistant before the start of the recruitment. The group allocation was kept in a sealed opaque envelope, which was only opened when a patient was enrolled. The assistant sent the target coordination according to the group allocation for each patient to TMS operators. Patients, assessors, TMS operators and other research staff were all blinded to the group allocations. The sample size was estimated according to a preliminary experiment with an expected effect size of 1.0 and a low dropout rate, yielding a minimum of 18 participants per group to achieve 80% power with an alpha level of 0.05. Group differences in baseline demographics and clinical characteristics of participants between the SCAN and effector groups were statistically assessed using two-tailed independent t-tests or Fisher's exact tests, as appropriate (Supplementary Table 5). One patient in the effector group discontinued stimulation owing to a scheduling conflict, leaving 17 patients in the group for outcome analysis. On each treatment day, two sessions of 1,800-pulse iTBS were administered at 50-min intervals in the morning and afternoon (Supplementary Fig. 13). In the SCAN group, all of the patients received stimulation in the middle SCAN region due to its easier accessibility to TMS. In the effector group, the patients received either foot or hand network stimulation according to the limb that was most affected. This was assessed by summing up the hand- and foot-related subscores of the MDS-UPDRS-III. Both groups received unilateral stimulation targeting the hemisphere contralateral to the side of the body with more severe motor symptoms. Stimulation targets were individualized based on personalized functional networks on the precentral gyrus identified using the patients' pretreatment scans. The stimulations were administered using an MT20A system (Neural Galaxy) equipped with a figure-of-eight coil, at 90% of the resting motor threshold (RMT). The RMT was defined as the minimum stimulation intensity required to elicit MEPs, recorded from the contralateral first dorsal interosseous muscle, with amplitudes ≥50 μV in at least 5 out of 10 consecutive trials. An experienced TMS operator, blinded to group assignment, identified the hand knob region based on anatomical landmarks and determined the motor hotspot for RMT without reference to the planned stimulation coordinates. The system also incorporates a real-time neuronavigation system to guide the placement of the coil throughout the stimulation procedure to ensure stimulation accuracy[101].

MRI acquisition. The same MRI scanner and parameters were used as in the PIPD dataset. In total, 900 functional image frames were collected from each participant, equivalent to 30 min, both before and after TMS treatment. The SCAN group had one patient who did not complete the follow-up scanning. Moreover, three patients from each group were excluded from the RSFC analysis owing to average relative head motion during scans greater than 0.25 mm, leaving 14 patients in each group.

DBS-ECoG dataset

Patients. This dataset was documented in a previous report[48]. In brief, 17 patients with PD (5 women, 12 men; mean ± s.d. age = 66.02 ± 6.33 years) who were candidates for STN DBS surgery were recruited at the University of Pittsburgh Medical Center. The protocol was approved by the local IRB (REN15020171/PRO13110420, 5 March 2015), and all of the participants provided written informed consent. Before the DBS surgery, dopaminergic medications were paused for 12 h. Before insertion of the microelectrodes, one or two subdural high-density ECoG arrays (63 channels, 3 × 21 contact array, 1-mm contact diameter, 3-mm separation; PMT) were temporarily placed on the left-hemisphere cerebral cortex. The ECoG strip locations were preoperatively planned to cover cortical regions of interest (ROIs), including the motor cortex.

STN stimulation and ECoG recording. Before starting the clinical microelectrode recordings, sedation was temporarily suspended, ensuring that the patients were at their standard neurological status as determined by clinical evaluations. Recordings were acquired using microprobe electrodes and monopolar stimulation of the STN was performed using a macro cylindrical contact (ring electrode, diameter 0.7 mm, length 1 mm) with the Neuro Omega stimulation software (Alpha Omega). After clinical assessments were concluded, anaesthesia monitoring was performed for at least 45 min. Subsequently, research-oriented stimulation was carried out at frequencies of 1 Hz for 30 s (totalling 30 stimulation pulses) and 10 Hz for 30 s (totalling 300 stimulation pulses) at intensities of 1, 2 and 3 mA at two different depths in the STN, each separated by at least 2 mm vertically. Concurrently with the stimulation, cortical evoked potentials were captured, amplified and digitalized using the Grapevine Neural Interface Processor (Ripple Neuro). The signals were captured at a 30 kHz sampling rate, with all of the channels referenced to a scalp ground.

The detailed approach to identify the locations of the ECoG strips was documented in a previous study[102]. The localization is based on preoperative stereotactic CT scans (General Electric, 9800) after placement of the Laksell frame, intraoperative fluoroscopy imaging (512 × 512 pixels, General Electric, OEC 9900) or CT imaging, and postoperative MRI (Siemens Allegra 1.5 T). Stereotactic CT images, either pre- or intra-operatively acquired, consisted of axial slices

with a thickness of 1.5 mm. MRI scans were performed using a T1w volumetric fast spoiled gradient echo (FSPGR) sequence (slice thickness = 1.5 mm, repetition time = 33.33 ms, echo time = 6 ms, flip angle = 35°).

MRgFUS dataset

Patients. A cohort of 10 patients with tremor-dominant PD (2 women, 8 men, mean ± s.d. age = 55.40 ± 7.24 years) was recruited for VIM-MRgFUS treatment at HPPH. The study was approved by the local IRB (2018-064-02, 29 December 2018), with ClinicalTrails.gov identifier NCT04002596. Written informed consent was obtained from all of the participating individuals. Inclusion criteria and clinical information for these patients were described in detail in our previous report[49]. MRgFUS was used to lesion the VIM contralateral to the most affected hand. The approximate target location was set on the anterior commissure (AC)– posterior commissure (PC) plane, at 75% of the AC–PC line and 14 mm lateral to the AC–PC line. When there was third ventricle enlargement, the approximate target was set to 11.5 mm lateral to the third ventricle wall.

MRI acquisition. MRI data were collected using the same MRI scanner and T1w and BOLD fMRI sequences as in the PIPD dataset. Moreover, T2w scans were collected the day after the MRgFUS intervention to image the brain lesions, using a 3 T MRI scanner (Discovery MR750, GE Healthcare) equipped with an 8-channel head coil (axial scans, TE = 98 ms, TR = 6,279 ms, flip = 111°, matrix = 288 × 384, FOV = 240 × 240 mm, slice thickness = 2 mm, slice interval = 2 mm, 31 slices; coronal scans, TE = 98 ms, TR = 6,264 ms, flip = 111°, FOV = 240 × 240 mm, matrix = 224 × 384, slice thickness = 2 mm, slice interval = 2 mm, 25 slices; sagittal scans, TE = 98 ms, TR = 6,268 ms, flip = 111°, FOV = 240 × 240 mm, matrix = 288 × 384, slice thickness = 2 mm, slice interval = 2 mm, 31 slices).

Lesion delineation. The MRgFUS lesions were manually delineated based on T1w and T2w images by a radiologist who was blinded to patients' clinical information using MRIcro (www.mccauslandcenter.sc.edu/mricro/). These lesions were subsequently overlapped to generate a lesion overlap map of the VIM target.

DBS-SS dataset

DBS sweet spots were extracted from a comprehensive retrospective multicohort DBS study[39]. In this dataset, there were 275 patients who underwent STN-DBS (80 women, 195 men, mean ± s.d. age = 59.8 ± 7.1 years), 28 patients with GPi-DBS (13 women, 15 men, mean ± s.d. age = 64.4 ± 7.0 years), and 39 patients with VIM-DBS (13 women, 26 men, mean ± s.d. age = 64.3 ± 11.6 years; Supplementary Table 1), following the IRB approval (15-9777). Written informed consent was obtained from all participants. Sweet spot atlases for STN-, GPi- and VIM-DBS were constructed based on probabilistic stimulation mapping, with sweet spots defined as voxels where the stimulation was consistently yielded above-average clinical improvement. The specific atlas used was the preinstalled version within the LEAD-DBS software[103]. We generated the target ROIs by applying a binary transformation to the probabilistic values of the sweet spot or overlap maps using a threshold greater than zero.

aDBS dataset

The aDBS dataset was reported in a previous study[28], including four male patients with PD (mean ± s.d. age = 58.50 ± 8.74 years), enrolled from the Departments of Neurology and Neurological Surgery at the University of California, San Francisco. The study was approved by the IRB of the University of California, San Francisco (18-24454, 2 August 2018) with ClinicalTrails.gov identifier NCT03582891. Written informed consent was obtained from all of the participants. Each patient underwent the bilateral STN-DBS implantation (Medtronic, 3389) along with the implantation of bilateral quadripolar subdural cortical electrode strips (Medtronic, 0913025) over the sensorimotor cortex. On the basis of a data-driven identification of optimal neural biomarkers of symptoms, cortical electrodes were used to extract real-time neural signals in three participants and four independently controlled hemispheres, serving as control signals in the aDBS control system. The remaining participant used subthalamic signals for adaptive control. Two patients received unilateral aDBS in the left hemisphere (patient 1 and patient 4) using cortical control, while the one other received independent bilateral aDBS using cortical control (patient 3), yielding six independent cortical hemispheres. The cortical electrode placements were identified by aligning postoperative CT scans with preoperative MRI. The locations of the electrodes were registered to the Montreal Neurological Institute (MNI) coordinate system. The study protocol is accessible at OSF (https://osf.io/cmndq/).

LCT dataset

Participants. A total of 21 patients with PD (mean ± s.d. age = 65.43 ± 4.12 years, 13 female individuals) were recruited to participate in a simplified LCT. The inclusion criteria included being aged between 40 and 75 years currently, with age ≥ 40 years at the time of diagnosis, and having a confirmed diagnosis of PD. Moreover, the participants must be in Hoehn–Yahr stages I–IV and show responsiveness to levodopa treatment, with a LCT improvement rate of ≥30%. The disease duration must be ≥3 years. Exclusion criteria comprised the following: (1) MRI contraindications; (2) Parkinson-plus syndromes or secondary parkinsonism; (3) a history of neuropsychiatric disorders aside from PD, including stroke, cerebrovascular disease, seizures and psychosis; (4) the presence of alcohol or other substance abuse; (5) inability to cooperate with MRI data collection. One patient was excluded owing to excessive head motion (mean relative motion >0.25 mm). The experimental protocol was approved by the IRB of Changping Laboratory (ER-25001-01, 17 April 2025). Written informed consent was obtained from all of the participants.

MRI acquisition. All MRI data were acquired using a 3 T GE SIGNA UHP scanner equipped with a 48-channel head coil at Changping Laboratory. In the medication off state (≥12 h after medication withdrawal), five rsfMRI runs (6 min each, totalling 30 min) were acquired with a gradient-echo EPI sequence (TR = 3,000 ms, TE = 30 ms, flip angle = 90°, voxel size = 3 × 3 × 3 mm^3, 47 axial slices). After the medication off scanning, the patient was instructed to take 150% of their regular morning levodopa dose by a neurologist from the Peking University First Hospital, and once peak motor response was jointly confirmed by the patient and the evaluator, the medication on scan was conducted using the same imaging protocol. Subsequently, structural images were collected using a 3D MPRAGE T1-weighted sequence with 1 mm isotropic resolution (192 sagittal slices, TR = 2,708 ms, TE = 3.5 ms, TI = 900 ms, flip angle = 8°, FOV = 256 × 256 mm^2). During all MRI sessions, the participants were instructed to keep their eyes closed, remain awake, minimize head motion and stay as still as possible.

ET dataset

Participants. A total of 45 patients with ET (mean ± s.d. age = 62.02 ± 13.10 years, 15 female individuals; Supplementary Table 7) were recruited from HPPH, China. The inclusion criteria included being aged 22 years or above and having a confirmed diagnosis of ET. Exclusion criteria comprised the following: (1) MRI contraindications; (2) the presence of any other neurodegenerative disease, such as Parkinson-plus syndromes; and (3) a history of neuropsychiatric disorders aside from ET, including stroke, cerebrovascular disease, seizures and psychosis. In total, 45 age- and sex-matched healthy participants (mean ± s.d. age = 58.28 ± 5.68 years, 19 female individuals) were sampled from the HC group from the PIPD dataset. Two male patients with ET were excluded owing to excessive head motion (mean relative motion >0.25 mm).

The experimental protocol was approved by the IRB of HPPH (2018-065-02, 29 December 2018). Written informed consent was obtained from all of the participants.

MRI acquisition. The MRI scanning protocol was identical to that used in the PIPD dataset.

Dystonia dataset

Participants. In total, 63 participants were enrolled, including 24 patients with laryngeal dystonia (LD, 4 abductor type, 20 adductor type; mean ± s.d. age = 60.5 ± 11.1 years, 17 female individuals), 18 patients with focal hand dystonia (FHD, mean ± s.d. age = 55.1 ± 14.6 years, 6 female individuals) and 21 HC individuals (mean ± s.d. age = 53.4 ± 12.7 years, 5 female individuals; Supplementary Table 8). The study was approved by the IRB of the Mass General Brigham (2017P002446/PHS, 22 January 2018), and all of the participants provided written informed consent in accordance with the Declaration of Helsinki. For all of the participants with focal dystonia, it had been at least 3 months since their last botulinum toxin injection and they were symptomatic during the performance of their dystonia-related tasks. Two participants from the LD group and one participant from the HC group were excluded from further analysis owing to excessive head motion during rsfMRI (mean relative motion > 0.25 mm).

MRI acquisition. Participants underwent one structural MRI scan, and four rsfMRI scans, each spanning 6 min, resulting in a cumulative scan duration of 20 min. MRI data were acquired using a 3 T Siemens Magnetom Prisma fit scanner equipped with a 32-channel head coil (Siemens Healthineers). T1-weighted structural imaging used a 3D MPRAGE sequence (TR = 2.5 s, TI = 1.0 s, 0.8 mm isotropic voxels, FOV = 256 mm, 208 sagittal slices, flip angle = 8°, bandwidth = 740 Hz per px). rsfMRI was obtained with a GE-EPI sequence (TR = 3,000 ms, TE = 30 ms, 3.0 mm isotropic voxels, FOV = 216 mm, 47 sagittal slices, flip angle = 85°, bandwidth = 2,240 Hz per px, echo spacing = 0.51 ms). During the resting-state scans, the participants were instructed to remain still with their eyes closed, stay awake and relax without focusing on any specific thoughts.

ALS dataset

Participants. In total, 30 patients with ALS (mean ± s.d. age = 59.52 ± 8.72 years; 14 female individuals) and 30 HC individuals (mean ± s.d. age = 62.68 ± 6.83 years, 15 female individuals; Supplementary Table 9) were enrolled. Inclusion criteria of ALS participant were: (1) current age between 40 and 80 years; (2) diagnosis of probable or higher-level motor neuron disease according to the revised El Escorial criteria; and (3) meeting the UMND ALS diagnostic criteria, presenting with upper motor neuron involvement in at least three segments and lower limb dysfunction with a Berg Balance Scale score below 40. Exclusion criteria were as follows: (1) MRI contraindications; (2) history of neurological or psychiatric disorders such as stroke, cerebrovascular disease, epilepsy or psychosis; (3) alcohol or other substance abuse; and (4) severe depression or anxiety (HAMD-17, ≥18; HAMA, ≥21). No participants were excluded for excessive head motion during rsfMRI (mean relative motion > 0.25 mm). The experimental protocol was approved by the IRB of Changping Laboratory (CPNL-IRB-0002-2, 21 June 2024). Written informed consent was obtained from all of the participants.

MRI acquisition. The MRI scanning protocol was identical to that used in the LCT dataset.

Clinical assessments

The primary outcome measure of patient motor symptoms was assessed using the UPDRS-III. In the DBS-fMRI dataset, the original version of the UPDRS-III was used in the medication off state, with patients refraining from taking medication for a minimum of 12 h before assessment. Subsequently, two experienced neurologists independently scored each UPDRS-III subitem based on recorded video material. Rigidity-related subitems were assessed by an on-site neurologist. These assessments exhibited substantial inter-rater reliability (ICC = 0.90)[104]. The scores used in this study represent the averages of the two assessors' scores. In the TMS dataset, the MDS-UPDRS-III[105] evaluations were conducted at the baseline as well as at 1 week and 2 weeks into treatment in the on-medication state. The primary and secondary outcomes were the changes in MDS-UPDRS-III score at the end of treatment (week 2 − baseline) and at week 1 (week 1 − baseline), respectively. These assessments were conducted by the same experienced neurologist who was blinded to the patients' group allocation. Moreover, we extracted specific subscores from the MDS-UPDRS-III to assess more targeted motor symptoms (Supplementary Table 4). In the PIPD and MRgFUS datasets, motor symptoms were evaluated in the on-medication state using the MDS-UPDRS-III. In the PIPD dataset, additional clinical assessments included the MMSE for cognitive function, the HAMD for depressive symptoms and the HAMA for anxiety symptoms. In the LCT dataset, motor symptoms were assessed using the MDS-UPDRS-III in both off and on medication states, conducted by the same neurologist from Peking University First Hospital to ensure consistency.

MRI preprocessing

The processing of both and structural data was conducted using the personalized Brain Functional Sectors (pBFS) Cloud v.1.0.7 (Neural Galaxy). The preprocessing pipeline, developed from our previously described pipeline[101,106,107], was adapted with software substitutions. The fMRI preprocessing sequence encompassed the following steps: (1) slice timing correction through stc_sess from the FreeSurfer v.6.0.0 software package (http://surfer.nmr.mgh.harvard.edu); (2) head motion correction using mc_sess from FreeSurfer (https://surfer.nmr.mgh.harvard.edu/fswiki/mc-sess); (3) linear detrending and bandpass filtering within the range of 0.01–0.08 Hz; and (4) regression to account for nuisance variables, which encompassed the six motion parameters, white matter signal, ventricular signal, global signal[108,109] and their first-order temporal derivatives.

For MP2RAGE T1w images of the PIPD, TMS and MRgFUS dataset, the brain was first extracted from the uniform T1-weighted image using Advanced Normalized Tools (ANTs)[110]. The subsequent preprocessing steps are consistent across structural sequences from the three datasets. The FreeSurfer v.6.0.0 software package (http://surfer.nmr.mgh.harvard.edu) was used for processing[111]. Surface mesh representations of the cerebral cortex were reconstructed from T1w images and non-linearly aligned to a shared spherical coordinate system. The functional and structural images were co-registered using boundary-based affine registration from the FsFast software package (http://surfer.nmr.mgh.harvard.edu/fswiki/FsFast). For the surface preprocessing pipeline, the functional images were aligned with the FreeSurfer cortical surface template (fsaverage6, 40,962 vertices per hemisphere). The fMRI surface data were smoothed by applying a 6-mm full-width half-maximum (FWHM) surface smoothing kernel. For the volumetric preprocessing pipeline, the preprocessed functional images in native space were normalized to a 2-mm spatial resolution volumetric template (the FSL version of the MNI ICBM152 non-linear template) using a co-registration matrix and volumetric non-linear registration with ANTs[110]. Then, a 6-mm FWHM isotropic smoothing Gaussian kernel was applied to the registered fMRI data within the brain mask.

RSFC analyses

In this study, we conducted three kinds of seed-based RSFC analyses. First, we performed cortico–cortical RSFC analysis to identify the SCAN inter-effector regions in participants. Second, we performed cortical RSFC analyses using seed ROIs derived from well-recognized subcortical regions in the widely accepted circuit models of PD

pathophysiology[3,5,19], including the SN, STN, thalamus/VIM, GPi, GPe and putamen using the HyraPD atlas[112,113]. The SN pars compacta (SNpc) and pars reticulata (SNpr) were combined into a single ROI—the SN—due to the limited spatial resolution of fMRI and the close anatomical proximity of these two structures. We also used seeds from the DBS sweet spot atlases. Lastly, we investigated whole-brain RSFC based on the seeds of the SCAN or the effector-specific network. To estimate the seed-based RSFC maps, we calculated Pearson correlations between the average BOLD fMRI signals within the seed ROI and the signals from cortical vertices or whole-brain voxels, in each participant. Subsequently, we converted the correlation coefficients (r values) into z values through Fisher's r-to-z transformation, normalizing the correlation coefficients. To generate group-averaged RSFC maps, we calculated the mean of the individualized z-maps across all participants in the group. To estimate cortical or whole-brain RSFC within a specific functional network or a ROI, we averaged the RSFC across all vertices within the network or region. To compare SCAN to effector RSFC (Fig. 1) or SCAN RSFC between patients with PD and HC individuals (Fig. 2) or changes in SCAN RSFC before and after treatment (Figs. 4 and 5), we averaged the RSFC across all six subcortical regions important in PD.

To assess differences in RSFC across networks, we used two-tailed paired t-tests when comparing RSFC between the SCAN, effector and other cortical networks. For group comparisons between patients with PD and healthy control individuals, we used two-tailed independent t-tests. Once we established that PD exhibited SCAN hyperconnectivity, we hypothesized that PD treatments would be associated with reduced hyperconnectivity. Thus, for longitudinal comparisons between the pretreatment baseline and post-treatment follow-up timepoints, including post-DBS, post-TMS and post-levodopa conditions, one-tailed paired t-tests were used, based on an a priori directional hypothesis that therapeutic STN-DBS, SCAN-targeted TMS and levodopa would reduce the SCAN hyperconnectivity observed in PD. To control for multiple comparisons across timepoints, networks or subcortical structures, FDR correction was applied.

Identification of the cortical SCAN regions

To identify the cortical SCAN regions, we performed a two-stage analysis consisting of an exploration stage and a network identification stage. First, to explore the existence of both individualized and group-level cortical SCAN regions, we placed a continuous line of seeds along the precentral gyrus and estimated their individual-specific or group-averaged RSFC, according to a previously described procedure[6]. Second, to delineate the personalized SCAN, we used an iterative precision functional mapping approach, as previously reported in detail[114–116]. In brief, the personalized functional parcellation was initiated from an atlas consisting of 17 group-average canonical functional networks and the SCAN from ref. 6. Each cortical vertex was assigned to one of the networks according to the correlation between the vertex's BOLD signal and the average BOLD signals of the 18 networks. The assignment was iteratively adjusted according to the same procedure described in ref. 114. Effector-specific network mapping was performed using the same procedure.

RSFC–symptom association analyses

To explore the relationship between SCAN-subcortical RSFC and both motor and non-motor symptoms, we performed separate partial least squares (PLS) regression analyses linking RSFC between six subcortical ROIs and the cortical SCAN to each of four clinical measures—MDS-UPDRS-III, MMSE, HAMA and HAMD—in the PIPD dataset. The regression analyses controlled confounds, including age, sex and disease severity measured by the Hoehn–Yahr scale. For each domain, we extracted the first latent variable (PLS1), which captures the optimal weighted combination of ROI-to-SCAN RSFC patterns and the corresponding symptom scores. We then assessed the strength of these associations using Pearson correlation between the RSFC-derived PLS1 scores and the clinical PLS1 scores for each symptom domain. To examine whether different symptom domains were associated with distinct subcortical connectivity profiles, we further calculated Spearman correlation between the PLS loadings (that is, weights of the six subcortical ROIs) derived from each symptom-specific model. The PLS analysis for MDS-UPDRS-III was replicated in the independent pretreatment data from the TMS dataset.

Winner-takes-all parcellation of subcortical structures

We followed a previously established winner-takes-all approach to parcellate subcortical structures that are important in PD into multiple functional networks corresponding to the large-scale cortical functional networks[51,117,118]. Specifically, we included the SN, STN, thalamus, GPi, GPe and striatum as delineated in the HybraPD atlas[112]. For each given voxel within these subcortical structures, we regressed out the average BOLD signals across cortical vertices within a 20-mm radius, thereby mitigating signal bleeding from adjacent cortical areas[51]. The functional connectivity between each subcortical voxel and all cortical networks of interest was then calculated. Each voxel, of which the functional connectivity with any network was significantly positive (one-sample t-tests, $P < 0.05$, uncorrected), was assigned to the functional network with the strongest connectivity. We performed an analysis using 11 functional networks, including the SCAN and 10 canonical functional networks[51]: the foot, hand, mouth, visual (VIS), action mode (AMN)[36], dorsal attention (DAN), ventral attention (VAN), default mode (DMN)[119], frontoparietal (FPN)[120] and salience (SAL)[121] networks. A Wilcoxon signed-rank test was performed to compare proportions of volume between the SCAN and effector-specific networks across six subcortical structures. To compare the proportions of voxels belonging to SCAN territory within six subcortical structures in patients versus control individuals, we conducted χ^2 tests for 11-network parcellations, FDR correcting for the six tests conducted.

Cortical evoked potential analyses

In the DBS-ECoG dataset, stimulation onsets were determined by identifying the initial time-bin with the largest voltage deflection in a channel exhibiting a significant stimulation artifact. Subsequently, the remaining ECoG channels were synchronized to these stimulation onsets, with each stimulation defining a trial. To filter out low-frequency fluctuations and avoid introducing filter artifacts, the raw voltage values for each trial were detrended by subtracting an eighth-order polynomial fit of the signal. For 1 Hz stimulation, 30 trials within each session were averaged for each channel and subsequently smoothed with a 5-bin (0.17 ms) moving window[122]. We then measured the amplitude and latency of positive voltage peak deflections after stimulation. To assess the antidromic activation of the hyperdirect pathway between the STN and cortex[48], we identified the cortical evoked potential 1 (P1) according to the previously reported approach[48]. Specifically, P1 was defined as the first positive voltage peak deflection occurring between 2 and 10 ms after stimulation onset, thereby excluding transcortical motor evoked potentials mediated by excitation of the corticospinal tract (<2 ms) and orthodromic activation through basal ganglia–thalamocortical pathways (> 2 ms).

We applied a two-step procedure to screen out ECoG electrodes of interest from 1,721 available ECoG electrodes and 9,147 voltage–time traces (Supplementary Fig. 9). First, we excluded electrodes without a well-defined P1 value. Second, it was observed that stimulation of the posterior-lateral STN yielded significantly higher evoked potential voltages in cortical areas proximal to the central sulcus[48]. We screened the most motor-related stimulation sites, following a procedure used in a previous report[48]. Specifically, we defined a one-dimensional STN axis using two points: the centre of the STN associative subregion (MNI coordinates = [−10.4, −11.7, −7.6] mm) and the centre of the STN motor subregion (MNI coordinates = [−12.6, −15.0, −7.1] mm). All STN stimulation

sites were projected onto this axis, and the most posterior-lateral sites (at the 50th percentile) were selected (Supplementary Fig. 9a). The screening procedure resulted in 1,174 unique ECoG electrodes and 2,160 traces (Supplementary Fig. 9b). The trace with the largest P1 was selected for each electrode from multiple corresponding traces stimulated using different parameter sets, including the stimulation site, frequency and intensity. To focus on M1 responses, we retained electrodes within the precentral gyrus label of the DKT atlas[123] only, yielding 284 electrodes—118 located in cortical SCAN regions and 166 in the mouth effector network (Supplementary Fig. 9b). For visualization of evoked traces, a zero-phase low-pass filter with a 2 kHz cut-off was applied to each mean voltage–time trace.

The probability distribution of the most responsive electrodes in the SCAN and mouth networks was examined using two-tailed χ^2 tests, with responsiveness thresholds ranging from the top 5% to 50% (Supplementary Fig. 9c). The P1 amplitudes of the most responsive electrodes in the SCAN and effector networks were compared using two-tailed independent sample *t*-tests. Furthermore, cluster-based permutation tests were performed to examine the differences in evoked traces between the two networks (Supplementary Fig. 9d), with multiple comparisons corrected at the cluster level. An alpha of 0.05 was defined as a cluster-building threshold, and 1,024 permutations were performed[124].

DBS electrode localization and VTA estimation

DBS electrode localization and VTA estimation were performed using the LEAD-DBS software[103]. Presurgical T1w MRI scans and post-surgical CT images were co-registered through linear registration to localize the electrodes according to a previously reported procedure[125]. Both CT and presurgical T1-weighted images were subsequently normalized to the MNI ICBM152 non-linear 2009b template using ANTs. Semi-automated identification of DBS electrode contacts was then performed on normalized CT images. The DBS electrodes from all 14 patients were reconstructed in MNI space[103].

Estimation of the VTA was performed according to a previously established procedure[126]. This process entailed generating a tetrahedral volume mesh based on the surface mesh of DBS contacts and subcortical regions using the Iso2Mesh toolbox within the LEAD-DBS software. Different regions were modelled as containing electrode materials, grey matter or white matter, with assigned conductivity values of 0.33 S m^{-1} and 0.14 S m^{-1}, respectively. For platinum/iridium contacts and insulated electrode segments, values of 108 S m^{-1} and 10,216 S m^{-1} were used, respectively. Using the volume conductor model, the potential distribution stemming from DBS was simulated through the integration of the FieldTrip-SimBio pipeline. The applied voltage to active electrode contacts served as a boundary condition. Subsequently, the gradient of the potential distribution was computed through finite element method (FEM) derivation. The resulting gradient, being piecewise continuous due to the application of first-order FEM, was thresholded for magnitudes surpassing the commonly used threshold of 0.2 V mm^{-1}. This delineated the extent and configuration of the VTA. To confirm that DBS stimulation site targeted appropriate locations, we examined the spatial overlapping, measured by Dice coefficient, between the VTA overlap across patients and the STN sweet spot from the DBS-SS dataset[39].

Patient-specific targeting procedure for TMS

Patient-specific TMS targets were generated based on personalized functional network mapping using pretreatment rsfMRI data from each participant[127], according to the procedure described in our previous reports[101,128,129]. First, the personalized SCAN and effector-specific motor regions were identified using the aforementioned personalized functional parcellation approach. Second, taking TMS accessibility into account, we restricted the candidate target searching area for each network in the precentral gyrus through excluding sulcal vertices and vertices in the medial surface. Third, we identified personalized targets in the candidate searching area based on the highest confidence value of the network parcellation. The confidence value of each vertex was estimated by ratio of the strongest and the second strongest correlation coefficient with all functional networks, indicating the likelihood of the vertex belonging to the assigned network. The automatically generated targets were visually inspected based on the anatomical locations and their RSFC patterns by two authors (J.R. and W.Z.), who were blinded to the group allocations.

TMS was delivered using a figure-of-eight coil. A real-time neuronavigation system incorporated in the TMS system was used throughout the procedure to ensure positioning accuracy. This system continuously monitored the positions of both the participant and the coil, and the TMS operator maintained coil positioning accuracy based on the real-time feedback. In practice, the distance between the coil centre and the cortical target was consistently maintained within 3 mm, and the angular deviation between the coil plane and the optimal tangential plane was kept within 3°. For orientation, a line normal to the longitudinal fissure within the coil plane was used as the reference axis, and the coil was rotated 45° around its normal[130].

LME models in DBS-fMRI and TMS analyses

To take advantage of the longitudinal DBS-fMRI dataset with multiple follow-up timepoints for each participant, we used three LME models to evaluate the DBS long-term effects on motor symptoms and RSFC. The UPDRS-III score served as the dependent variable, with follow-up timepoints (from preoperative to 1-, 3-, 6- and 12-month postoperative assessments) defined as a fixed effect, and participant identity as a random effect. Post hoc pairwise *t*-tests were conducted to compare the preoperative scores and the postoperative scores. Similarly, an LME model was applied to the RSFC of the SCAN circuit. Moreover, an LME model was used to investigate the relationship between changes in clinical outcomes and STN-SCAN RSFC across different follow-up visits. The dependent variable was the observed change rate in UPDRS-III scores, while the fixed effects included the change rate of STN-SCAN RSFC and the follow-up timepoints; participant was also considered as a random effect.

In the TMS study, the rTMS effect on motor symptoms or RSFC was evaluated among participants who had at least one post-treatment assessment[131]. An LME model was used to assess the effects on motor symptoms of different stimulation targets on score changes across all clinical assessments, including the MDS-UPDRS-III total scores (Fig. 5b) and four subdomains of motor symptoms (Extended Data Fig. 8). Fixed effects included stimulation target group (SCAN or effector), time of assessment (baseline, week 1, week 2), and their interaction, with disease duration, levodopa equivalent dose (LEDD) and baseline Hoehn–Yahr staging as covariates. Participant identification was the random effect. Similarly, an LME model was used to evaluate the changes in RSFC of the SCAN circuit.

Distance analysis of aDBS cortical electrodes

To investigate the spatial relationship between cortical electrodes of aDBS and the cortical SCAN nodes, we compared the distances from the cortical electrodes to the centres of the superior SCAN node with the distance from the electrodes to the hand and foot regions. The centre position for each network in each hemisphere was determined based on the group-averaged centre coordinates of personalized functional networks across 166 patients with PD from the PIPD dataset. In the six hemispheres from four patients, four cortical electrode pairs in four hemispheres from three patients (patient 1, 3 and 4) were eventually selected for adaptive stimulation[28]. We then calculated the Euclidean distances from each cortical electrode pair to the corresponding hemispheric network centres and averaged the distances across the electrode pairs.

MRgFUS target distance estimation

To determine the theoretically optimal target within the thalamus using SCAN functional connectivity, we used a cluster-based strategy, which was adapted from a method previously used to identify individualized rTMS targets in the dorsolateral prefrontal cortex for depression[132] and in the superior frontal gyrus for post-stroke aphasia[101]. We specifically identified contiguous thalamic voxel clusters that exhibited the highest connectivity correlation with the SCAN regions. The centre of gravity of the largest such cluster was determined as the optimal target coordinate. We quantified the Euclidean distance between this optimal target coordinate and the actual target coordinate, which was determined by the centre of gravity of each patient's lesion. Moreover, as part of our control analyses, this method was applied to other effector-specific networks including the foot, hand and mouth networks, as well as a combination of the three networks. We calculated the Spearman correlation between MDS-UPDRS-III scores changes (before − after) and the Euclidean distance between the SCAN-based optimal target and the actual target. Spearman correlations were also calculated using the distance between the optimal target based on foot, hand and mouth networks or a combination of all effector-specific networks.

Reporting summary

Further information on research design is available in the Nature Portfolio Reporting Summary linked to this article.

Data availability

The anonymized data from the PIPD and ET dataset are available at the Science Data Bank (https://doi.org/10.57760/sciencedb.28929 and https://doi.org/10.57760/sciencedb.28935, respectively). The DBS-ECoG data are available at the Harvard Dataverse website (https://doi.org/10.7910/DVN/CNI25V). Individual patient data from the DBS-fMRI data are a part of clinical trials and not publicly available now but will be made available in other clinical data repositories. The patient data from the TMS, MRgFUS, LCT, dystonia and ALS datasets are available from the corresponding authors on request to maintain anonymity. The locations of cortical electrodes of the aDBS dataset are available on the Data Archive for the BRAIN Initiative website (https://dabi.loni.usc.edu/; https://doi.org/10.18120/cq9c-d057). The probability maps of sweet spots of DBS targets of the DBS-SS dataset are available at GitHub (https://github.com/netstim/leaddbs/tree/master/templates). The volumetric brain template is an ultrahigh-resolution ex vivo brain in MNI space[133], which is available at Dryad (https://datadryad.org/stash/downloads/file_stream/182489); the DISTAL atlas is available online (https://www.lead-dbs.org/helpsupport/knowledge-base/atlasesresources/distal-atlas/). The HybraPD atlas is available online (https://www.lead-dbs.org/helpsupport/knowledge-base/atlasesresources/atlases-2/). Source data are provided with this paper.

Code availability

All fMRI data were preprocessed using a cloud medical image data processing software, pBFS cloud, available online (https://app.neuralgalaxy.cn/research/). Code specific to analyses can be found at GitHub (https://github.com/pBFSLab/SCAN_PD). Software packages incorporated into the above code for data analysis included: Python v.3.7 (https://www.python.org); MATLAB R2020b (https://www.mathworks.com/); Connectome Workbench v.1.5 (http://www.humanconnectome.org/software/connectome-workbench.html); Freesurfer v.6.0.0 (https://surfer.nmr.mgh.harvard.edu/); FSL v.6.0 (https://fsl.fmrib.ox.ac.uk/fsl/fslwiki); ANTs v.0.3.8 (https://github.com/ANTsX/ANTs); and LeadDBS v.2.0 (https://www.lead-dbs.org/).

99. Ren, J., Bai, Y., Wang, M. & Liu, H. Precision Imaging Parkinson's Disease (PIPD) dataset. *Sci. Data Bank* https://doi.org/10.57760/sciencedb.28929 (2025).
100. Ren, J., Bai, Y., Wang, M. & Liu, H. Precision Imaging Essential Tremor (PIET) dataset. *Sci. Data Bank* https://doi.org/10.57760/sciencedb.28935 (2025).
101. Ren, J. et al. Personalized functional imaging-guided rTMS on the superior frontal gyrus for post-stroke aphasia: a randomized sham-controlled trial. *Brain Stimul.* **16**, 1313–1321 (2023).
102. Randazzo, M. J. et al. Three-dimensional localization of cortical electrodes in deep brain stimulation surgery from intraoperative fluoroscopy. *Neuroimage* **125**, 515–521 (2016).
103. Horn, A. et al. Lead-DBS v2: towards a comprehensive pipeline for deep brain stimulation imaging. *Neuroimage* **184**, 293–316 (2019).
104. Shen, L. et al. Subthalamic nucleus deep brain stimulation modulates 2 distinct neurocircuits. *Ann. Neurol.* **88**, 1178–1193 (2020).
105. Goetz, C. G. et al. Movement Disorder Society-sponsored revision of the Unified Parkinson's Disease Rating Scale (MDS-UPDRS): scale presentation and clinimetric testing results. *Mov. Disord.* **23**, 2129–2170 (2008).
106. Ren, J. et al. Dissociable auditory cortico-cerebellar pathways in the human brain estimated by intrinsic functional connectivity. *Cereb. Cortex* **31**, 2898–2912 (2021).
107. Ren, J. et al. Individual variability in functional organization of the human and monkey auditory cortex. *Cereb. Cortex* **31**, 2450–2465 (2021).
108. Ciric, R. et al. Benchmarking of participant-level confound regression strategies for the control of motion artifact in studies of functional connectivity. *Neuroimage* **154**, 174–187 (2017).
109. Satterthwaite, T. D. et al. Motion artifact in studies of functional connectivity: characteristics and mitigation strategies. *Hum. Brain Mapp.* **40**, 2033–2051 (2017).
110. Wu, J. et al. Accurate nonlinear mapping between MNI volumetric and FreeSurfer surface coordinate systems. *Hum. Brain Mapp.* **39**, 3793–3808 (2018).
111. Fischl, B. FreeSurfer. *Neuroimage* **62**, 774–781 (2012).
112. Yu, B. et al. HybraPD atlas: towards precise subcortical nuclei segmentation using multimodality medical images in patients with Parkinson disease. *Hum. Brain Mapp.* **42**, 4399–4421 (2021).
113. Poldrack, R. A. Region of interest analysis for fMRI. *Soc. Cogn. Affect. Neurosci.* **2**, 67–70 (2007).
114. Wang, D. et al. Parcellating cortical functional networks in individuals. *Nat. Neurosci.* **18**, 1853–1860 (2015).
115. Li, M. et al. Performing group-level functional image analyses based on homologous functional regions mapped in individuals. *PLoS Biol.* **17**, e2007032 (2019).
116. Wang, D. et al. Individual-specific functional connectivity markers track dimensional and categorical features of psychotic illness. *Mol. Psychiatry* **25**, 2119–2129 (2020).
117. Choi, E. Y., Yeo, B. T. & Buckner, R. L. The organization of the human striatum estimated by intrinsic functional connectivity. *J. Neurophysiol.* **108**, 2242–2263 (2012).
118. Buckner, R. L., Krienen, F. M., Castellanos, A., Diaz, J. C. & Yeo, B. T. The organization of the human cerebellum estimated by intrinsic functional connectivity. *J. Neurophysiol.* **106**, 2322–2345 (2011).
119. Fox, M. D. et al. The human brain is intrinsically organized into dynamic, anticorrelated functional networks. *Proc. Natl Acad. Sci. USA* **102**, 9673–9678 (2005).
120. Marek, S. & Dosenbach, N. U. F. The frontoparietal network: function, electrophysiology, and importance of individual precision mapping. *Dialogues Clin. Neurosci.* **20**, 133–140 (2022).
121. Seeley, W. W. et al. Dissociable intrinsic connectivity networks for salience processing and executive control. *J. Neurosci.* **27**, 2349–2356 (2007).
122. Miocinovic, S. et al. Cortical potentials evoked by subthalamic stimulation demonstrate a short latency hyperdirect pathway in humans. *J. Neurosci.* **38**, 9129–9141 (2018).
123. Klein, A. & Tourville, J. 101 labeled brain images and a consistent human cortical labeling protocol. *Front. Neurosci.* **6**, 171 (2012).
124. Maris, E. & Oostenveld, R. Nonparametric statistical testing of EEG- and MEG-data. *J. Neurosci. Methods* **164**, 177–190 (2007).
125. Horn, A. & Kuhn, A. A. Lead-DBS: a toolbox for deep brain stimulation electrode localizations and visualizations. *Neuroimage* **107**, 127–135 (2015).
126. McIntyre, C. C., Grill, W. M., Sherman, D. L. & Thakor, N. V. Cellular effects of deep brain stimulation: model-based analysis of activation and inhibition. *J. Neurophysiol.* **91**, 1457–1469 (2004).
127. Lynch, C. J. et al. Automated optimization of TMS coil placement for personalized functional network engagement. *Neuron* **110**, 3263–3277 (2022).
128. Tang, Z. et al. Efficacy and safety of high-dose TBS on poststroke upper extremity motor impairment: a randomized controlled trial. *Stroke* **55**, 2212–2220 (2024).
129. Ren, J. et al. Efficacy and safety of high-dose and personalized TBS on post-stroke cognitive impairment: a randomized controlled trial. *Brain Stimul.* **18**, 249–258 (2025).
130. Gomez-Tames, J., Hamasaka, A., Laakso, I., Hirata, A. & Ugawa, Y. Atlas of optimal coil orientation and position for TMS: a computational study. *Brain Stimul.* **11**, 839–848 (2018).
131. Gratton, C., Lee, T. G., Nomura, E. M. & D'Esposito, M. The effect of theta-burst TMS on cognitive control networks measured with resting state fMRI. *Front. Syst. Neurosci.* **7**, 124 (2013).
132. Cash, R. F. H. et al. Personalized connectivity-guided DLPFC-TMS for depression: advancing computational feasibility, precision and reproducibility. *Hum. Brain Mapp.* **42**, 4155–4172 (2021).
133. Edlow, B. L. et al. 7 Tesla MRI of the ex vivo human brain at 100 micron resolution. *Sci. Data* **6**, 244 (2019).

Acknowledgements We thank Y. Li for drawing illustrative figures (Figs. 1a and 3a and Extended Data Figs. 9a and 10) and D. Liu for data collection. This work was supported by the Changping Laboratory (H.L.); National Institutes of Health grants MH096773 (N.U.F.D.), MH122066 (E.M.G. and N.U.F.D.), MH121276 (E.M.G. and N.U.F.D.), MH124567 (E.M.G. and N.U.F.D.), NS129521 (E.M.G. and N.U.F.D.), NS088590 (N.U.F.D.), R01NS131405 (S. Little),

U01NS098969 (R.M.R.) and U01NS117836 (R.M.R.); the National Natural Science Foundation of China 81527901 (L.L.), 81720108021 (M.W.), 81971689 (G.-J.J.), 31970979 (K.W.), and 82090034 (K.W.), the National Key R&D Program of China grants 2017YFE0103600 (M.W.); the Intellectual and Developmental Disabilities Research Center (N.U.F.D.); by the Kiwanis Foundation (N.U.F.D.); the Washington University Hope Center for Neurological Disorders (E.M.G. and N.U.F.D.); and the Collaborative Innovation Center of Neuropsychiatric Disorders and Mental Health of Anhui Province grant2020xkjT05 (K.W.).

Author contributions Conception: J.R. and H.L. Design: J.R., W.Z. and H.L. Data acquisition, analysis and interpretation: J.R., W.Z., L.D., E.M.G., S.L., Y. Zhou, Y.L., J. Huang, Yafei Zhu, N.G., C.J., F.Z., Y.B., W. Wei, Y.W., A.B., M.V., L.W., C.R.O., M.A.M., C.Z., Q.H., Ying Zhu, Y.Y., W.C., X.F., P.Z., W. Wang, G.-J.J., J. He, D.F., K.W., Z.W., T.K., S.L., P.A.S., R.M.R., L.L., M.W., D.W., N.U.F.D. and H.L. Manuscript writing and revision: J.R., W.Z., L.D., E.M.G., D.W., N.U.F.D. and H.L.

Competing interests H.L. is the chief scientist of Neural Galaxy. C.J. serves on the scientific advisory board for Beijing Pins Medical. C.J. is listed as an inventor in issued patents and patent applications on the deep brain stimulator used in this work. N.U.F.D. has a financial interest in Turing Medical and may financially benefit if the company is successful in marketing FIRMM motion monitoring software products. E.M.G. and N.U.F.D. may receive royalty income based on FIRMM technology developed at Washington University School of Medicine and licensed to Turing Medical. N.U.F.D. is a co-founder of Turing Medical. These potential conflicts of interest have been reviewed and are managed by Washington University School of Medicine. S.L. consults for Iota Biosciences. P.A.S. receives support from Medtronic and Boston Scientific for fellowship education. The other authors declare no competing interests.

Additional information

Supplementary information The online version contains supplementary material available at https://doi.org/10.1038/s41586-025-10059-1.

Correspondence and requests for materials should be addressed to Jianxun Ren, Meiyun Wang, Danhong Wang or Hesheng Liu.

Peer review information *Nature* thanks Alfonso Fasano, Wolf-Julian Neumann, Alberto Priori and the other, anonymous, reviewer(s) for their contribution to the peer review of this work. Peer reviewer reports are available.

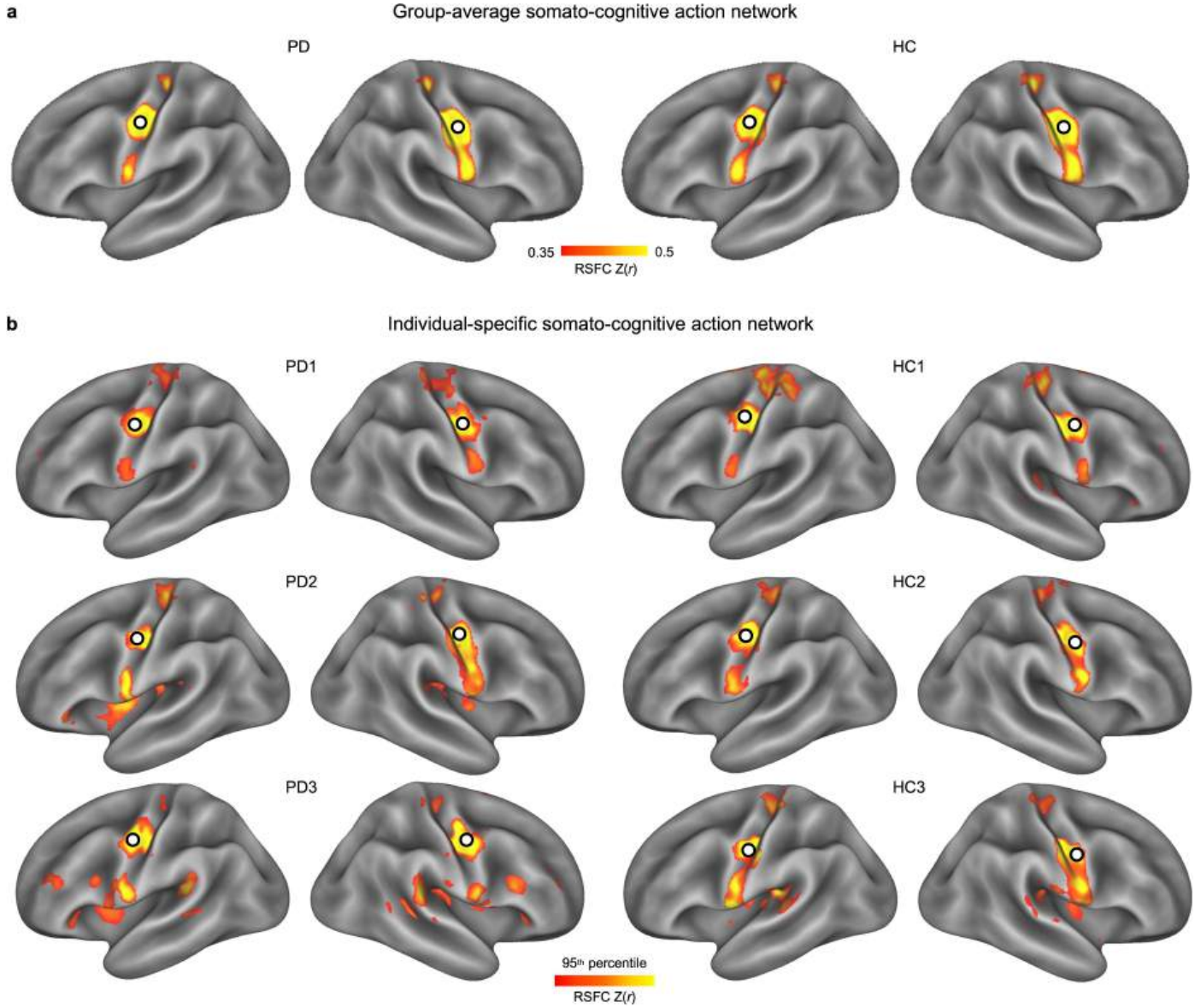

Extended Data Fig. 1 | The SCAN (somato-cognitive action network) motif in Parkinson's disease (PD) and healthy older individuals. The characteristic (SCAN) motif, consisting of three distinct inter-effector regions within the primary motor cortex (M1) strip of each hemisphere, can be observed consistently at the group level in **a**, PD patients (left; PIPD dataset, $n = 166$) and healthy older participants (right; $n = 60$), as well as at the individual level in **b**, PD patients (left; PD1-PD3) and healthy control individuals (right; HC1-HC3, age > 65 years). Circles indicate the seed regions of interest located in the middle inter-effector region of the SCAN.

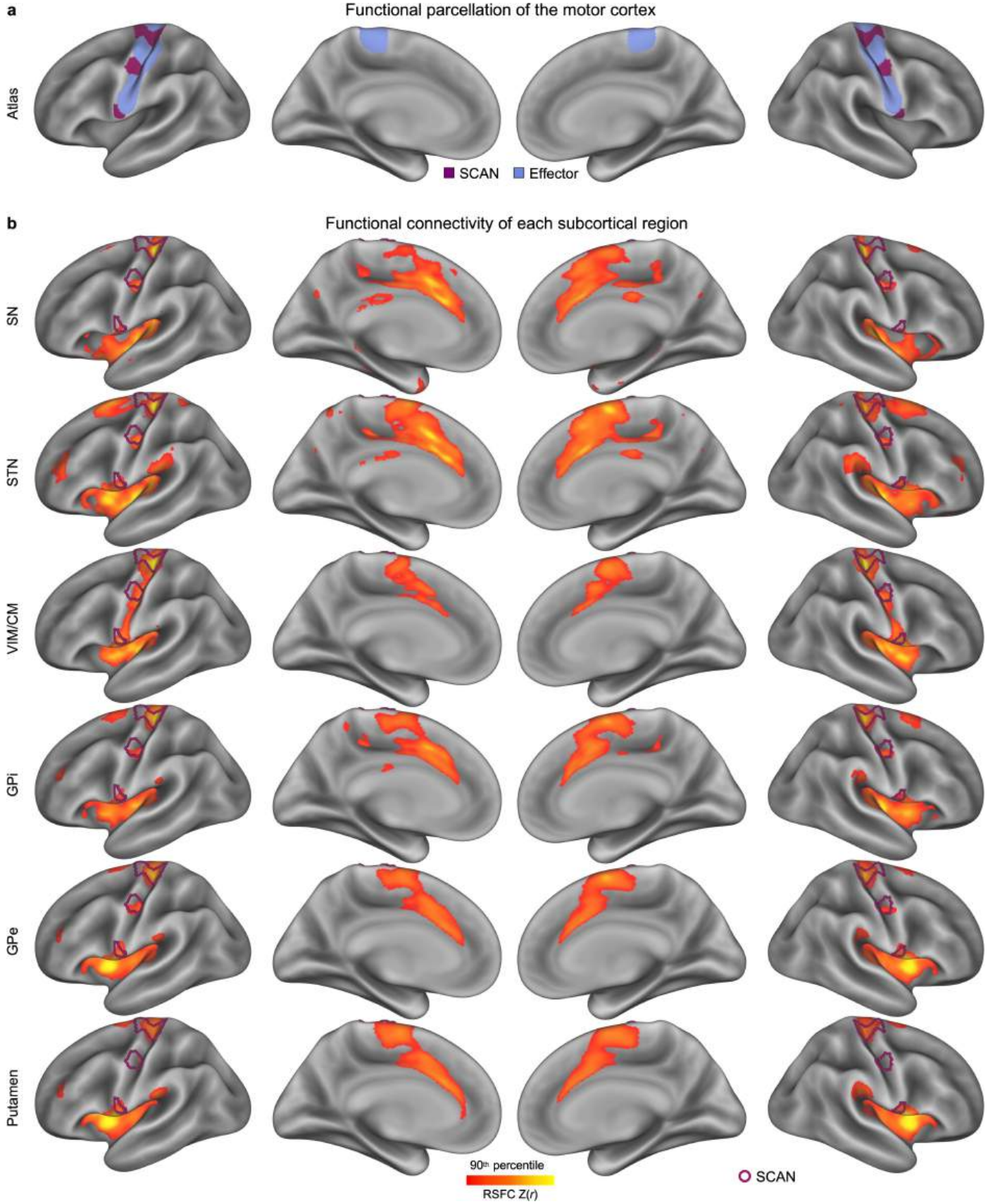

Extended Data Fig. 2 | See next page for caption.

Extended Data Fig. 2 | Functional connectivity between subcortical regions and the cortical networks in Parkinson's disease (PD) patients. **a**, Functional networks of interest are delineated on cortical surfaces: the somato-cognitive action network (SCAN, purple) and the effector motor regions (blue) including the foot, hand, and mouth networks. The SCAN is mapped through fine-grained functional parcellation. **b**, The functional connectivity map of each of the six subcortical regions (SN, STN, VIM/CM, GPi, GPe, and putamen) were derived using data from 166 PD patients, consistent with Fig. 1c, but the maps are displayed in comprehensive views, including lateral and medial views of left and right hemispheres. These maps highlight the top 10 percent of cortical vertices with the strongest connectivity. The purple outlines highlight strong functional connectivity in the SCAN.

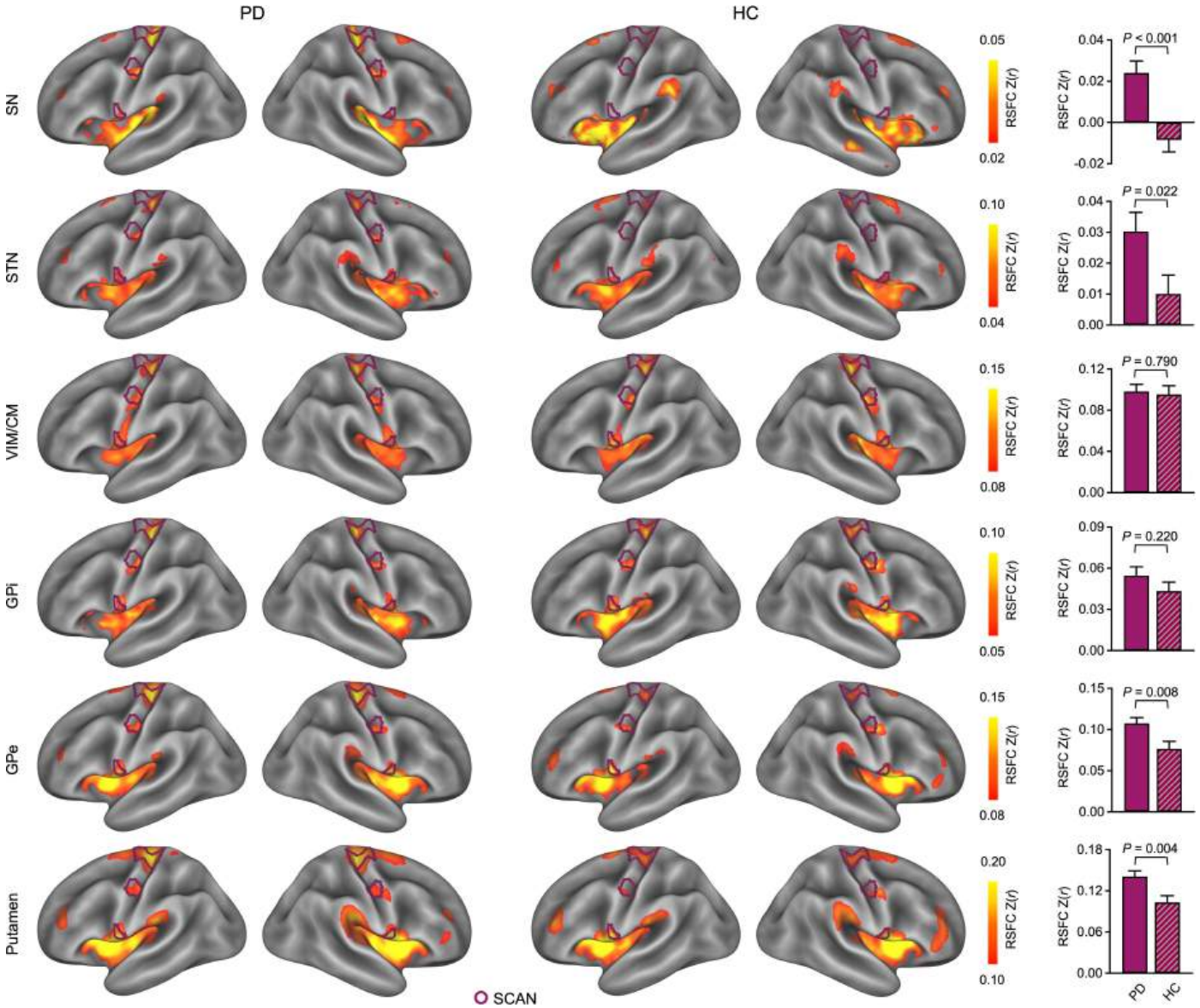

Extended Data Fig. 3 | Hyperconnectivity between subcortical structures and the SCAN (somato-cognitive action network) in PD. Functional connectivity maps of each of the six subcortical regions (SN, STN, VIM/CM, GPi, GPe, and putamen) are derived using data from 65 PD patients (a subset of the 166 PD patients; left) and 60 demographically matched healthy control individuals (HC; right). The maps are displayed using the same functional connectivity thresholds for the two groups, allowing for direct comparison. Lateral views of both the left and right hemispheres are depicted, with SCAN boundaries overlaid. The putamen ($P = 0.004$), GPe ($P = 0.008$), STN ($P = 0.022$), and SN ($P = 0.0001$) show significantly stronger functional connectivity with the SCAN in PD patients compared to healthy control individuals (one-tailed independent t-tests, $P < 0.05$). However, there is no significant between-group differences in the VIM/CM ($P = 0.395$) and GPi ($P = 0.110$) and connectivity with the SCAN. The different trends between significant regions (SN, STN, GPe, and putamen) and non-significant regions (GPi and VIM/CM) may reflect distinct subcircuits, as revealed by our previous DBS-evoked task activations[104]. Data are presented as mean ± s.e.m.

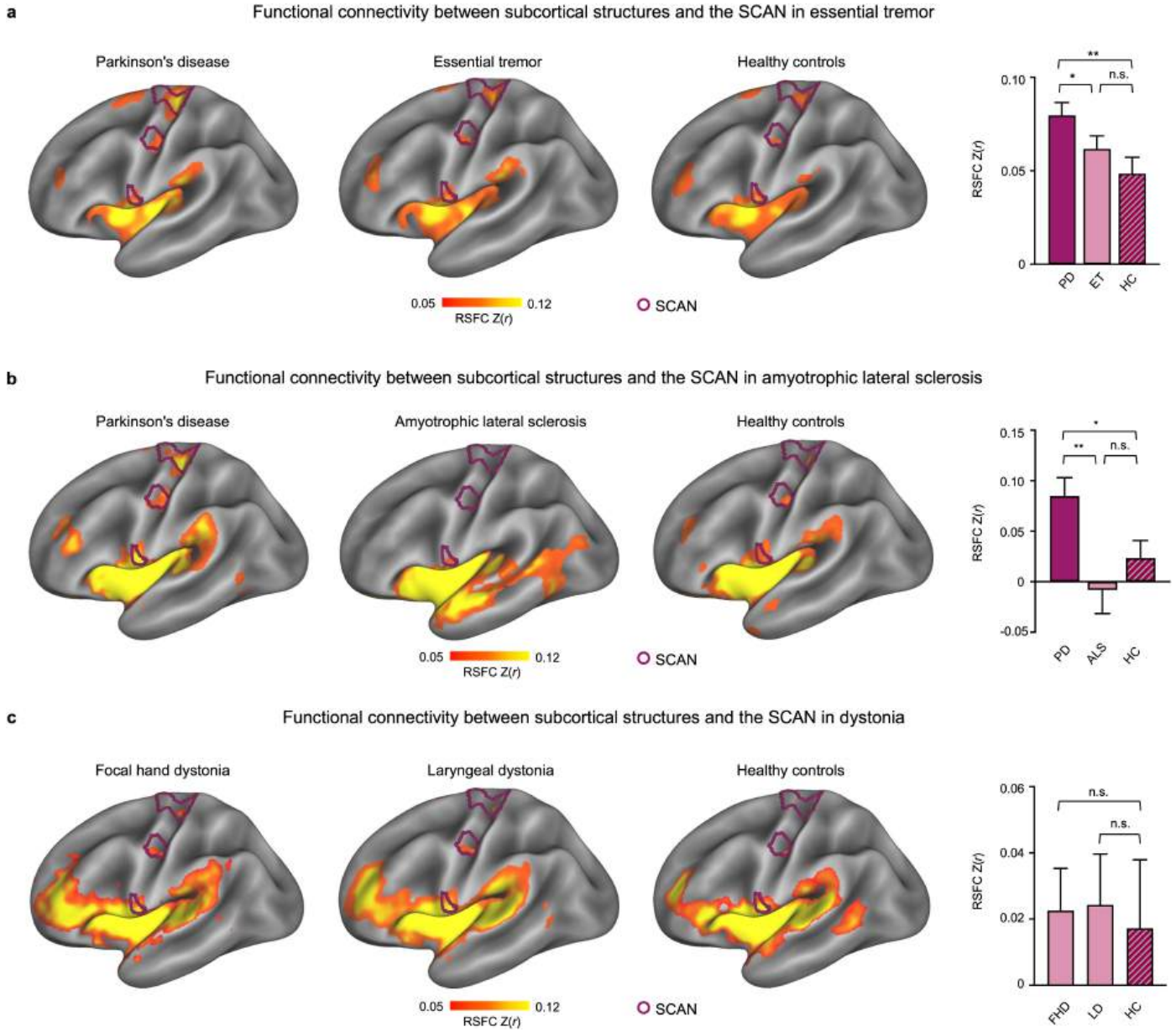

Extended Data Fig. 4 | Hyperconnectivity between subcortical structures and SCAN is absent in essential tremor, amyotrophic lateral sclerosis and dystonia. a, Left: the average resting-state functional connectivity (RSFC) maps of the six subcortical nodes (SN, STN, VIM, GPi, GPe, putamen) in patients with Parkinson's disease (PD, $n = 65$), essential tremor (ET, $n = 43$), and healthy control individuals (HC, $n = 45$). All participants were scanned with the same scanner and parameters at Henan Provincial People's Hospital. All maps are displayed with the same RSFC threshold to allow direct comparison. Lateral views of the left hemisphere are shown with SCAN boundaries overlaid. Right: The bar plot shows mean RSFC between the subcortical nodes and the SCAN. PD exhibited significantly higher connectivity than both ET ($P = 0.034$) and HC ($P = 0.006$), while no significant difference was observed between ET and HC ($P = 0.242$). **b**, Left: RSFC maps of the same six subcortical nodes in patients with PD ($n = 20$), ALS ($n = 30$), and HC ($n = 30$), whose data were collected with the same scanner at Changping Laboratory. Right: the bar plot shows significantly higher RSFC in PD compared to both ALS ($P = 0.007$) and HC ($P = 0.021$), but no significant difference between ALS and HC ($P = 0.265$). **c**, Left: Group-average RSFC maps from the same six subcortical nodes in patients with focal hand dystonia (FHD, $n = 18$), laryngeal dystonia (LD, $n = 22$), and HC ($n = 20$) scanned at Massachusetts General Hospital. Right: the bar plot shows no significant differences between either dystonia group and HC ($P > 0.05$). All statistical comparisons were performed using two-tailed independent t-tests. $^*P < 0.05$, $^{**}P < 0.01$, n.s. = not significant. All data are presented as mean ± s.e.m.

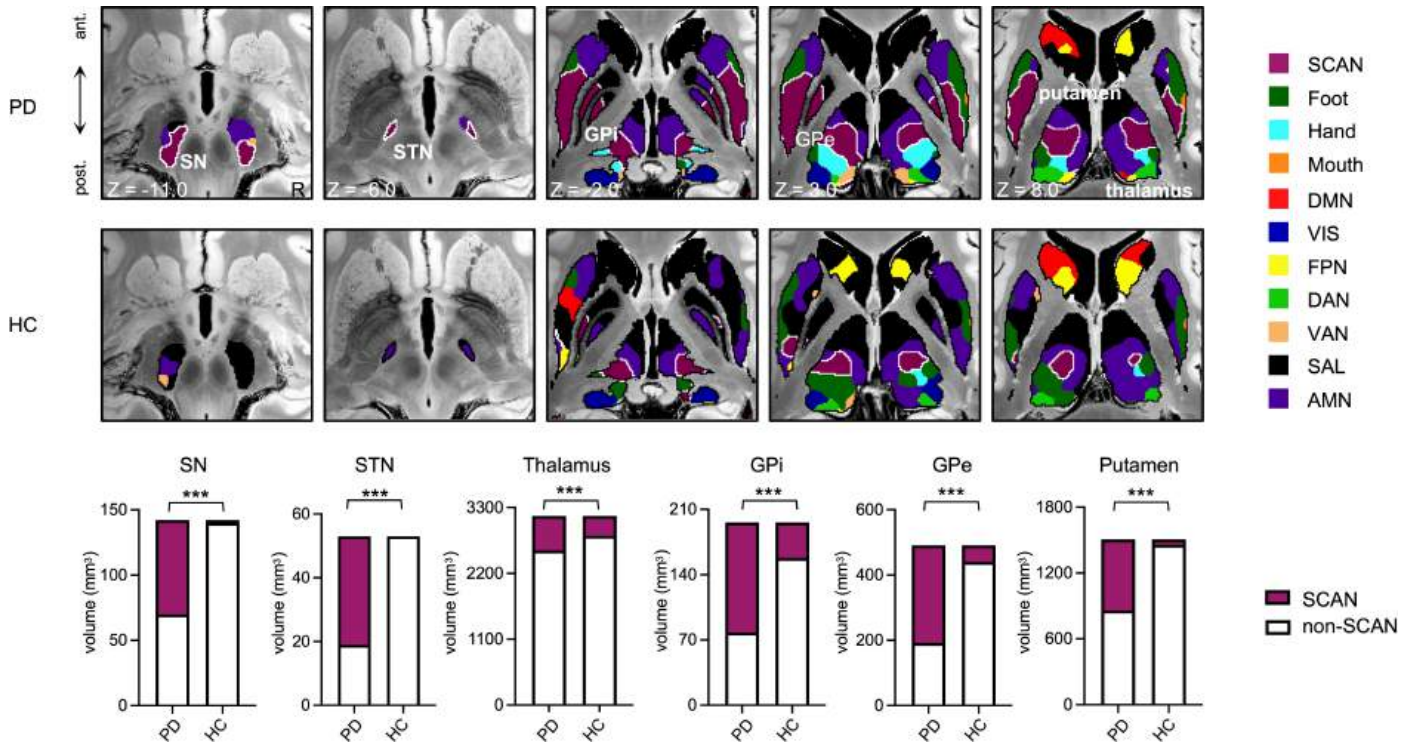

Extended Data Fig. 5 | Winner-take-all functional network parcellation in Parkinson's disease (PD) patients compared to healthy control individuals. Each voxel within the subcortical regions was assigned to one of eleven canonical functional networks, based on its RSFC with these networks[51] (see Methods). In PD patients, the SCAN, highlighted by white boundaries, predominantly localized to the posterior SN, posterior STN, VIM/CM of the thalamus, posterior GPi, posterior GPe, and posteromedial putamen. The motor effector regions (foot, hand, mouth) showed consistently less representation across all subcortical regions (Wilcoxon signed-rank test, $P = 0.031$). The identical winner-take-all parcellation procedure was applied to healthy participants. The parcellation of healthy control individuals showed smaller SCAN representations than PD patients for each subcortical region. The proportions of the SCAN in five out of six subcortical structures were significantly higher in PD patients compared to healthy control individuals (two-tailed χ^2 tests, SN: $^{***}P = 1.08 \times 10^{-20}$; STN: $^{***}P = 6.56 \times 10^{-12}$; Thalamus: $^{***}P = 1.00 \times 10^{-18}$; GPi: $^{***}P = 3.59 \times 10^{-16}$; GPe: $^{***}P = 7.43 \times 10^{-61}$; Putamen: $^{***}P = 8.56 \times 10^{-148}$; FDR-corrected). The enlargements of the SCAN representations in the subcortical regions are in line with the cortico-subcortical hyperconnectivity in PD patients.

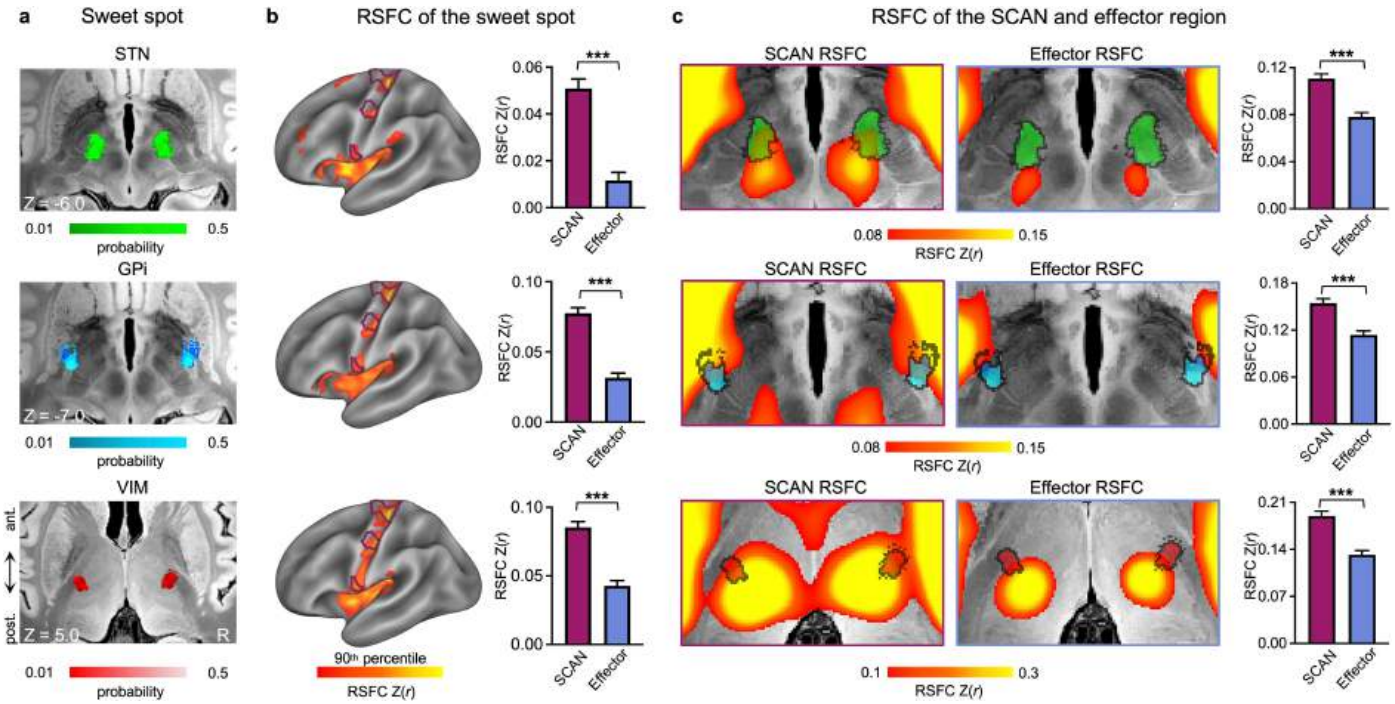

Extended Data Fig. 6 | Functional connectivity of effective DBS targets. **a**, Sweet spots of three distinct DBS targets for Parkinson's disease (PD), including the STN (green), GPi (blue), and VIM (red), were identified from a multi-centre study (DBS-SS dataset, $n = 342$; Supplementary Table 1)[39]. **b**, Left, the corresponding cortical RSFC maps exhibit functional connectivity patterns similar to the SCAN (somato-cognitive action network). Right, the bar graphs show that the functional connectivity with the SCAN is significantly stronger than with effector-specific regions for all DBS sweet spots (PIPD dataset, $n = 166$; all two-tailed paired t-tests, STN: $P = 1.10 \times 10^{-28}$; GPi: $P = 1.25 \times 10^{-32}$; VIM: $P = 1.10 \times 10^{-28}$, FDR-corrected). Data are presented as mean ± s.e.m. **c**, Group-averaged resting-state functional connectivity (RSFC) maps of PD patients derived from the seeds in the SCAN cortical regions and effector-specific regions. Left, the DBS sweet spots are overlaid on these RSFC maps. The SCAN RSFC maps exhibit greater overlap with the targets compared to those of the effector-specific regions. Right, each target is more strongly connected to the SCAN than to the effector-specific regions (all two-tailed paired t-test, STN: $P = 1.12 \times 10^{-24}$; GPi: $P = 1.19 \times 10^{-20}$; VIM: $P = 2.05 \times 10^{-26}$, $^{***}P < 0.001$, FDR-corrected), indicating that these effective DBS targets are selectively connected with the SCAN. The results were replicated in the DBS-fMRI dataset (see Supplementary Fig. 8). Data are presented as mean ± s.e.m.

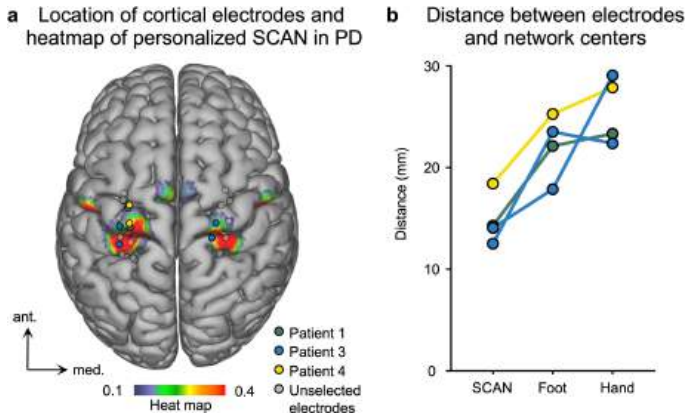

Extended Data Fig. 7 | Proximity of adaptive DBS (aDBS) cortical electrodes to SCAN (somato-cognitive action network). a, In the aDBS cohort, four Parkinson's disease (PD) patients underwent aDBS surgery, with cortical electrode strips used for closed-loop neuromodulation in four independent hemisphere and three of four patients[28]. The electrodes were projected and are shown in the MNI surface space, overlaid on a heat map showing the overlap of personalized SCAN. Personalized SCAN was delineated using individual rsfMRI data for each of 166 PD patients from the PIPD dataset (see Methods), and the heat map represents the overlap of SCAN across these patients. Four cortical electrode pairs in four hemispheres from three patients (Patient 1, 3, and 4) were selected for adaptive stimulation. Selected electrodes majorly overlapped with the superior SCAN node. Unselected electrodes are shown in semi-transparent grey. **b**, The box plot illustrates the average Euclidean distances between the centres of the networks (superior SCAN node, Foot, and Hand) and the selected cortical electrodes in each hemisphere. The cortical electrodes are closer to the superior SCAN node compared to the foot and hand networks.

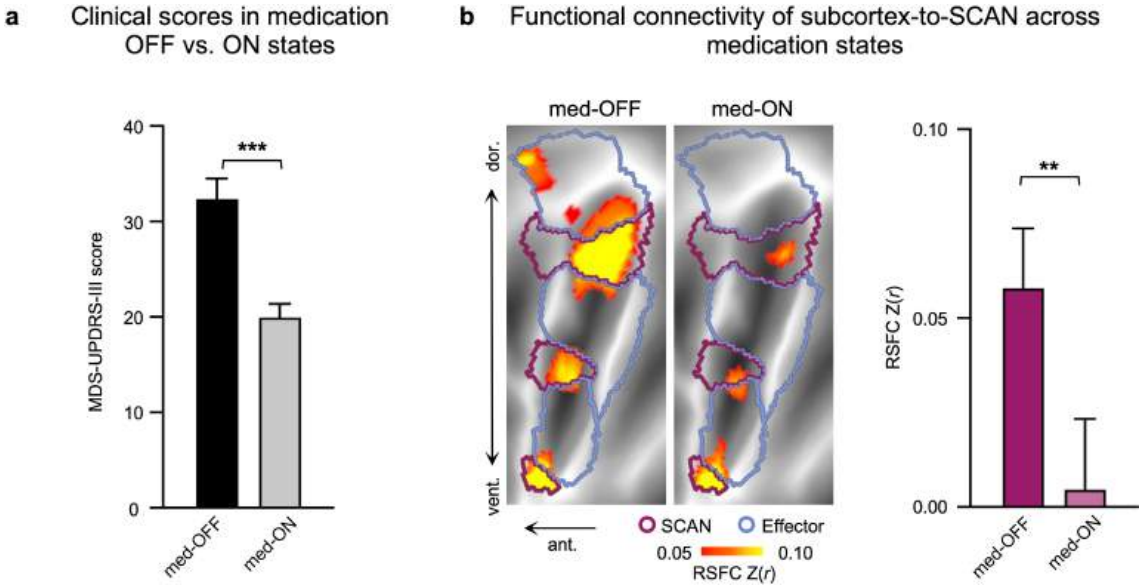

Extended Data Fig. 8 | Effects of dopaminergic medication on SCAN (somato-cognitive action network) hyperconnectivity in Parkinson's. **a**, In a simplified levodopa challenge test ($n = 20$; see Methods), levodopa significantly reduced overall motor symptoms, as measured by the MDS-UPDRS-III (Unified Parkinson's Disease Rating Scale Part III; one-tailed paired t-test, $t = 7.18$, $^{***}P = 4.00 \times 10^{-7}$). **b**, Left, group-average cortical functional connectivity maps seeded from subcortical regions are shown on flattened M1 surfaces, revealing stronger connectivity with the SCAN (purple outlines) than with effector-specific regions (blue outlines). Right, bar plots show that levodopa significantly reduced SCAN-subcortex hyperconnectivity ($n = 20$; one-tailed paired t-test, $t = 3.58$, $^{**}P = 0.001$). Data are presented as mean ± s.e.m.

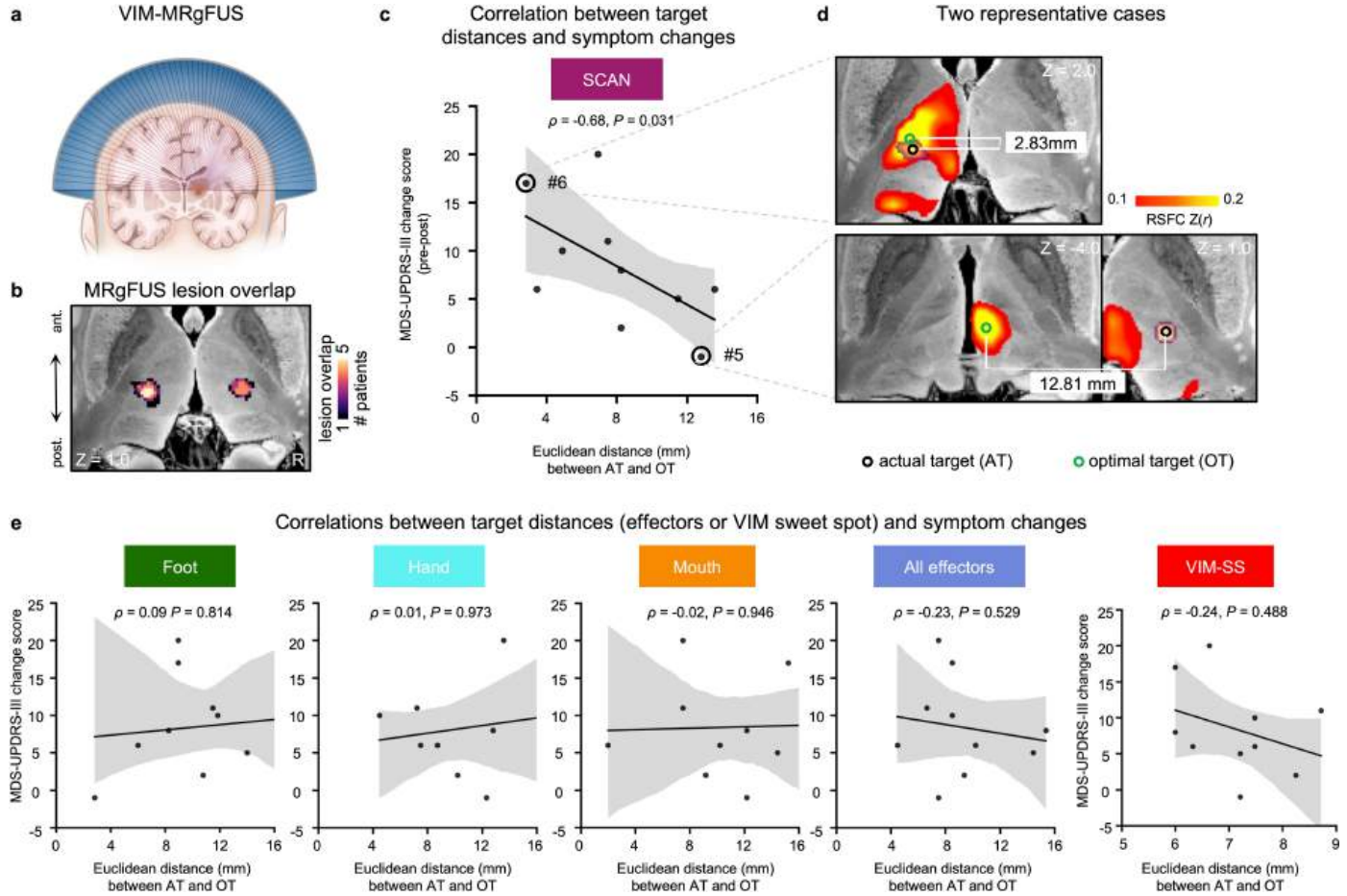

Extended Data Fig. 9 | Association between closeness to functionally-defined SCAN targets and clinical outcomes in focused ultrasound for tremor. a, An illustration shows the application of MR-guided focus ultrasound stimulation (MRgFUS) to the VIM. **b**, Ten tremor-dominant Parkinson's disease (PD) patients received MRgFUS to ablate the VIM contralateral to the most affected hand. The map shows the overlap of lesions across patients. **c**, Optimal target (OT) of each patient was identified as the gravity centre of the largest cluster in the thalamus functionally connected to the cortical SCAN regions (resting-sate functional connectivity, RSFC). The Euclidean distances between the OT and actual targets (AT) are anti-correlated with the changes of overall motor symptoms (two-tailed Spearman correlation, $\rho = -0.68$, $P = 0.031$), suggesting that targets closer to the SCAN hotspot yielded better responses. The shaded areas represent 95% confidence intervals of the mean estimate. **d**, Two representative patients (#5 and #6) are highlighted. Patient #6 showed a large response to the MRgFUS (MDS-UPDRS-III change score = 17) with a short distance (2.83 mm) between AT (black circle) and OT (green circle). In contrast, patient #5 exhibited a poor response (change score = −1) with a greater distance (12.81 mm) between the AT and OT. **e**, Control analyses were conducted by defining the OT using connectivity with the foot, hand, and mouth network, a combination of all effector-specific motor networks, or VIM sweet spot (VIM-SS). None of these analyses showed a significant correlation between the distances and clinical responses (two-tailed Spearman correlations, $P > 0.05$). The shaded areas represent 95% confidence intervals of the mean estimate.

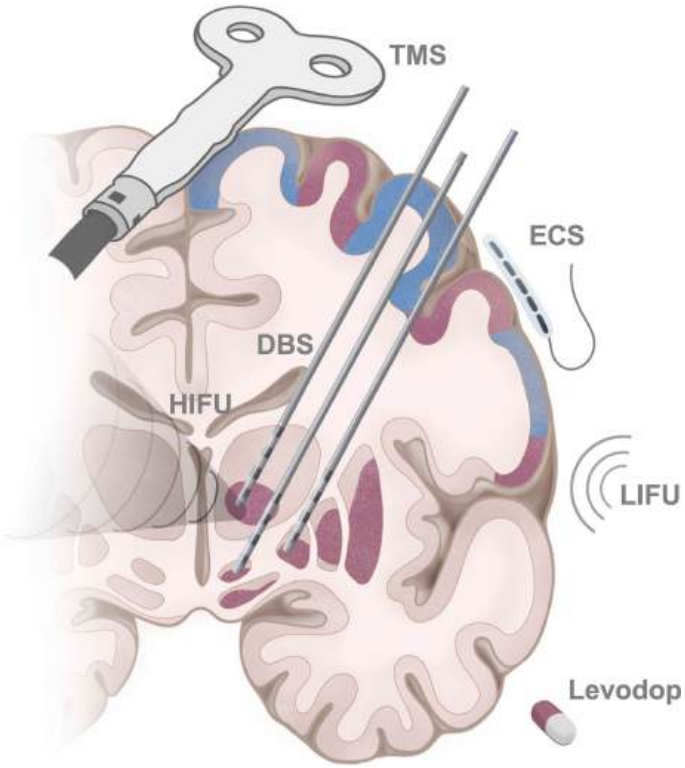

Extended Data Fig. 10 | SCAN-targeted medications and neuromodulatory therapies for Parkinson's disease (PD). An illustration depicts multiple types of circuit-based therapies focusing on the SCAN (somato-cognitive action network) for PD treatment. The cortical and subcortical regions in the SCAN are represented in purple. Various neuromodulation techniques, including transcranial magnetic stimulation (TMS), deep brain stimulation (DBS), high-intensity focused ultrasound (HIFU), low-intensity focused ultrasound (LIFU), and potentially electrical cortical stimulation (ECS) targeting the SCAN circuit, hold the potential for alleviating PD symptoms.

Extended Data Table 1 | Data utilized: characteristics and imaging information

Dataset		Demographics				fMRI information		
		Sample size	Sex	Age mean(std)	Disease duration (yr) mean(std)	Session	Duration /session(mins)	Total duration (mins)
PIPD	Patient (full sample)[a]	166	64F/102M	61.8(7.8)	5.8(4.1)	1	30	4980
	Patient (subset)[b]	65	28F/37M	58.6(8.6)	5.1(2.8)	1	30	1950
	Control	60	34F/26M	56.1(6.6)	-	1	30	1800
	p-val	-	0.18[c,e]	0.08[d,e]	-	-	-	-
DBS-fMRI	Patient	14	5F/9M	54.7(7.7)	9.7(4.0)	5	Pre-op: 30 Post-op: 24	5796
	Control	25	13F/12M	56.3(6.9)	-	1	19	475
	p-val	-	0.52[c]	0.50[d]	-		-	-
TMS	Patient	36	13F/23M	65.1(6.8)	4.9(3.3)	2	30	2160
DBS-ECoG	Patient	17	5F/12M	66.0(6.3)	-	-	-	-
MRgFUS	Patient	10	2F/8M	55.4(7.2)	5.2(1.7)	2	30	600
DBS-SS	Patient	342	106F/236M	60.7(7.6)	13.7(6.1)	-	-	-
aDBS	Patient	4	4M	58.5(8.7)	12.3(2.2)	-	-	-
LCT	Patient	21	13F/8M	65.4(4.12)	7.8 (3.8)	2	30	1200
ET	Patient	45	15F/30M	62.0(13.1)	10.6(8.7)	1	30	1290
	Control	45	19F/26M	58.3(5.7)	-	1	30	1350
	p-val	-	0.48[c]	0.09[d]	-		-	-
Dystonia	FHD	18	6F/12M	55.1(14.6)	18.7(15.3)	1	24	432
	LD	24	17F/7M	60.5(11.1)	17.3(10.7)	1	24	528
	Control	21	5F/16M	53.4(12.7)	-	1	30	480
	p-val	-	0.02[c]	0.07[d]	-		-	-
ALS	Patient	30	14F/16M	59.5 (8.7)	-	1	30	900
	Control	30	15F/15M	62.7 (6.8)	-	1	30	900
	p-val	-	0.80[c]	0.12[d]	-	-	-	-

[a]: The full sample of the PIPD dataset includes 166 patients with PD.
[b]: Sixty-five patients with PD were subsampled to match the demographics information with healthy control individuals.
[c]: Chi-square test.
[d]: Two-tailed independent *t*-test.
[e]: Comparisons between 65 patients with PD and 60 healthy control individuals.

nature portfolio

Corresponding author(s): Hesheng Liu, Jianxun Ren

Last updated by author(s): Nov 17, 2025

Reporting Summary

Nature Portfolio wishes to improve the reproducibility of the work that we publish. This form provides structure for consistency and transparency in reporting. For further information on Nature Portfolio policies, see our Editorial Policies and the Editorial Policy Checklist.

Statistics

For all statistical analyses, confirm that the following items are present in the figure legend, table legend, main text, or Methods section.

n/a	Confirmed	
☐	☒	The exact sample size (*n*) for each experimental group/condition, given as a discrete number and unit of measurement
☐	☒	A statement on whether measurements were taken from distinct samples or whether the same sample was measured repeatedly
☐	☒	The statistical test(s) used AND whether they are one- or two-sided *Only common tests should be described solely by name; describe more complex techniques in the Methods section.*
☐	☒	A description of all covariates tested
☐	☒	A description of any assumptions or corrections, such as tests of normality and adjustment for multiple comparisons
☐	☒	A full description of the statistical parameters including central tendency (e.g. means) or other basic estimates (e.g. regression coefficient) AND variation (e.g. standard deviation) or associated estimates of uncertainty (e.g. confidence intervals)
☐	☒	For null hypothesis testing, the test statistic (e.g. *F*, *t*, *r*) with confidence intervals, effect sizes, degrees of freedom and *P* value noted *Give P values as exact values whenever suitable.*
☒	☐	For Bayesian analysis, information on the choice of priors and Markov chain Monte Carlo settings
☒	☐	For hierarchical and complex designs, identification of the appropriate level for tests and full reporting of outcomes
☐	☒	Estimates of effect sizes (e.g. Cohen's *d*, Pearson's *r*), indicating how they were calculated

Our web collection on statistics for biologists contains articles on many of the points above.

Software and code

Policy information about availability of computer code

Data collection	Data was sourced from multiple sites, as explained in the manuscript and in the Data section below. MRI data was collected from MRI scanners, no software or code was used.
Data analysis	All fMRI data were preprocessed using a cloud medical image data processing software, personalized Brain Functional Sectors (pBFS) Cloud v1.0.7 (Neural Galaxy Inc., Beijing), at https://app.neuralgalaxy.cn/research Code specific to analyses can be found at https://github.com/pBFSLab/SCAN_PD Software packages incorporated into the above code for data analysis included: Python v3.7, https://www.python.org Matlab R2020b, https://www.mathworks.com/ Connectome Workbench 1.5, http://www.humanconnectome.org/software/connectome-workbench.html Freesurfer v6.0.0, https://surfer.nmr. mgh.harvard.edu/ FsFast v4.0, http://surfer.nmr.mgh.harvard.edu/fswiki/FsFast FSL v6.0, https://fsl.fmrib.ox.ac.uk/fsl/fslwiki ANTs v0.3.8 https://github.com/ANTsX/ANTs LeadDBS v2.0, https://www.lead-dbs.org/ Neuro Omega stimulation software (Alpha Omega Co, Alpharetta, GA, USA) Grapevine Neural Interface Processor (Ripple Neuro, Salt Lake City, UT, USA) MRIcro v1.39 https://www.mccauslandcenter.sc.edu/mricro/)

For manuscripts utilizing custom algorithms or software that are central to the research but not yet described in published literature, software must be made available to editors and reviewers. We strongly encourage code deposition in a community repository (e.g. GitHub). See the Nature Portfolio guidelines for submitting code & software for further information.

Data

Policy information about availability of data

All manuscripts must include a data availability statement. This statement should provide the following information, where applicable:

- Accession codes, unique identifiers, or web links for publicly available datasets
- A description of any restrictions on data availability
- For clinical datasets or third party data, please ensure that the statement adheres to our policy

The anonymized data from the PIPD and ET dataset are available at https://doi.org/10.57760/sciencedb.28929 and https://doi.org/10.57760/sciencedb.28935, respectively.
The DBS-ECoG data are available on the Harvard Dataverse website at https://doi.org/10.7910/DVN/CNI25V.
Individual patient data from the DBS-fMRI data are a part of clinical trials and not publicly available now but will be made available in other clinical data repositories.
The patient data from the TMS, MRgFUS, LCT, dystonia and ALS datasets are available from the corresponding authors upon request because of maintenance of anonymity.
The locations of cortical electrodes of the aDBS dataset are available on the Data Archive for the BRAIN Initiative website (https://dabi.loni.usc.edu/; https://doi.org/10.18120/cq9c-d057).
The probability maps of sweet spots of DBS targets of the DBS-SS dataset are available at https://github.com/netstim/leaddbs/tree/master/templates.
The volumetric brain template is an ultrahigh-resolution ex-vivo brain in MNI space, which is available at https://datadryad.org/stash/downloads/file_stream/182489; the DISTAL atlas is available at https://www.lead-dbs.org/helpsupport/knowledge-base/atlasesresources/distal-atlas/.
The HybraPD atlas is available at https://www.lead-dbs.org/helpsupport/knowledge-base/atlasesresources/atlases-2/.

Research involving human participants, their data, or biological material

Policy information about studies with human participants or human data. See also policy information about sex, gender (identity/presentation), and sexual orientation and race, ethnicity and racism.

Reporting on sex and gender	Findings apply to all studied individuals and groups, regardless of sex. Sex ratios: PIPD: 226 (98F, 128M) DBS-fMRI: 39 (18F, 21M) TMS: 36 (13F, 26M) DBS-ECoG: 17 (5F, 12M) MRgFUS: 10 (2F, 8M) DBS-SS: 342 (106F, 236M) aDBS: 4 (0F, 4M) LCT: 21 (8M, 13F) ET: 90 (56M, 34F) Dystonia: 63 (35M, 28F) ALS: 60 (34M, 29F)
Reporting on race, ethnicity, or other socially relevant groupings	No socially constructed or socially relevant categorization variables were used or are relevant for our manuscript.
Population characteristics	Findings apply to all studied individuals and groups, regardless of age. Age ranges: For each dataset the population characteristics are summarized below: PIPD: mean age = 59.0, standard deviation = 7.2 years DBS-fMRI: mean age = 55.5, standard deviation = 7.3 years TMS: mean age = 65.1, standard deviation = 6.8 years DBS-ECoG: mean age = 66.0, standard deviation = 6.3 years MRgFUS: mean age = 55.4, standard deviation = 7.2 years DBS-SS: mean age = 60.7, standard deviation = 7.6 years aDBS: mean age = 58.5, standard deviation = 8.7 years LCT: mean age = 65.4, standard deviation = 4.1 years ET: mean age = 60.2, standard deviation = 9.4 years Dystonia: mean age = 56.3, standard deviation = 12.8 years ALS: mean age = 61.1, standard deviation = 7.8 years
Recruitment	Participants across all datasets were recruited from clinical centers through standard clinical referral pathways and voluntary participation. Across all datasets, recruitment was based on voluntary participation, which introduces potential self-selection bias, as individuals willing to participate in research may differ systematically from those who decline (e.g., higher motivation, milder symptoms, or better tolerance for MRI procedures). PIPD: The PD patients and healthy participants were recruited from Henan Provincial People's Hospital (HPPH), China. DBS-fMRI: This dataset is a part of the 3T MRI-compatible DBS cohort. The PD patients were recruited from three centers, including Tiantan Hospital, Beijing; Peking Union Medical College Hospital, Beijing; and Qilu Hospital, Jinan, China. Healthy

control participants matched in age to the patient group were recruited.
TMS: All participants were recruited at HPPH from 29 May, 2023 to 28 April, 2024.
DBS-ECoG: 17 patients with PD who were candidates for STN DBS surgery were recruited at the University of Pittsburgh Medical Center.
MRgFUS: A cohort of 10 patients with tremor-dominant PD were recruited for VIM-MRgFUS treatment at HPPH.
DBS-SS: DBS sweet spots were extracted from a comprehensive retrospective multicohort DBS study. The patients who underwent DBS surgery at Toronto Western Hospital prior to 2018 were recruitment.
aDBS: Four male PD patients enrolled from the Departments of Neurology and Neurological Surgery at the University of California, San Francisco.
LCT: A total of 21 PD patients were recruited to participate in a simplified LCT at Changping laboraty, Beingjing, China.
ET: A total of 45 ET patients were recruited from HPPH, China.
Dystonia: Sixty-three participants, including 24 patients with laryngeal dystonia, 18 patients with focal hand dystonia, and 21 healthy controls were enrolled from Massachusetts General Hospital, Charlestown, MA, USA.
ALS: Thirty patients with ALS (mean age = 59.52 ± 8.72 years; 14 females) and 30 healthy controls (mean age = 62.68 ± 6.83 years, 15 females; Supplementary Table 9) were enrolled from Beijing, China.

Ethics oversight

All data were acquired with IRB approval at their original institutions.
PIPD: The experimental protocol was approved by the HPPH Institutional Review Board.
DBS-fMRI: The ethics approval for this project was granted by the ethics committees of Tiantan Hospital (QX2016-009-02, 21 July, 2016), Peking Union Medical College Hospital (HS2016094, 21 September, 2016), and Qilu Hospital (2016008, 28 August, 2016).
TMS: The study protocol was approved by the institutional ethics committee of HPPH (2023LS37, 7 May, 2023).
DBS-ECoG: The protocol was approved by the local IRB (REN15020171/PRO13110420, 5 March, 2015), and all participants provided written informed consent.
MRgFUS: The study was approved by the local IRB (2018-064-02, 29 December, 2018).
DBS-SS: The study was approved by the IRB approval (15-9777).
aDBS: The study was approved by the IRB of the University of California, San Francisco (18-24454, 2 August 2018).
LCT: The experimental protocol was approved by the IRB of Changping Laboratory (ER-25001-01, 17 April 2025). Written informed consent was obtained from all participants.
ET: The experimental protocol was approved by the IRB of HPPH (2018-065-02, 29 Dec 2018). Written informed consent was obtained from all participants.
Dystonia: The study was approved by the IRB of the Mass General Brigham (2017P002446/PHS, 22 Jan 2018), and all participants provided written informed consent in accordance with the Declaration of Helsinki.
ALS: The experimental protocol was approved by the IRB of Changping Laboratory (CPNL-IRB-0002-2, 21 June 2024). Written informed consent was obtained from all participants.

Note that full information on the approval of the study protocol must also be provided in the manuscript.

Field-specific reporting

Please select the one below that is the best fit for your research. If you are not sure, read the appropriate sections before making your selection.

☒ Life sciences ☐ Behavioural & social sciences ☐ Ecological, evolutionary & environmental sciences

For a reference copy of the document with all sections, see nature.com/documents/nr-reporting-summary-flat.pdf

Life sciences study design

All studies must disclose on these points even when the disclosure is negative.

Sample size

We used eleven independent datasets comprising 863 total participants after quality control. These datasets include 1) PIPD dataset: 166 patients with PD and 60 healthy controls, 2) DBS-fMRI dataset: 14 patients with PD, with evaluations conducted both pre- and post-DBS surgery, along with 25 healthy controls, 3) TMS dataset: 36 patients with PD, 4) DBS-SS dataset: 342 patients with PD, 5) DBS-ECoG dataset: 17 PD patients who underwent STN-DBS surgery and DBS-evoked ECoG recording, 6) MRgFUS dataset: 10 patients with tremor-dominant PD, 7) aDBS dataset: 4 PD patients, 8) LCT dataset: 21 patients with PD, 9) essential tremor dataset: 45 patients with essential tremor and 45 healthy controls from the PIPD dataset, 10) dystonia dataset: 42 patients with dystonia and 21 healthy controls, and 11) ALS datastet: 30 patients with ALS and 30 healthy controls.The main focus of this study is on analyzing the differences between PD patients and the healthy control group. This multi-center, multi-modal dataset can ensure the accuracy and reliability of the research results.
No formal statistical sample-size calculation was performed for the datasets included in this study. Sample sizes were determined based on the availability of eligible participants at each clinical center, the feasibility constraints of advanced neuroimaging and neuromodulation procedures (including DBS, MRgFUS, and TMS), and consistency with sample sizes reported in prior studies using comparable designs. For the large-scale fMRI and clinical cohorts (e.g., PIPD, ET, dystonia, ALS), the achieved sample sizes are substantially larger than those used in previous published work and are sufficient to ensure stable group-level estimates and robust functional connectivity analyses. For the TMS dataset, data followed a rigorous sample size estimation procedure to ensure sufficient statistical power under the predefined effect size and significance level. For the DBS-related cohorts (DBS-fMRI, DBS-ECoG, aDBS, MRgFUS, DBS-SS), sample sizes reflect typical recruitment numbers in highly specialized surgical populations, where enrollment is inherently constrained by strict clinical eligibility criteria. Although these sample sizes are modest, they are in line with the literature and sufficient to detect reproducible stimulation-evoked neural responses and to support individualized circuit-level analyses. Together, the sample sizes across all datasets are appropriate for the study aims and consistent with established standards in the field.

Data exclusions

PIPD: 4 PD patients did not complete MRI scanning, and 10 patients were excluded due to excessive head motion. 11 participants due to excessive head motion were excluded.

PIPD: Four patients did not complete MRI scanning, and 10 patients were excluded due to excessive head motion. After excluding 11 healthy participants due to excessive head motion.
DBS-fMRI: 1 participant was excluded due to incomplete MRI data caused by discomfort in the scanner, and 2 participants because of excessive head motion.
TMS: 3 patients from each group were excluded from the RSFC analysis due to average relative head motion during rs-fMRI scans greater than 0.25 mm, leaving 14 patients in each group.
LCT: One patient was excluded due to excessive head motion (mean relative motion > 0.25 mm).
ET: Two male ET patients were excluded due to excessive head motion (mean relative motion > 0.25 mm).
Dystonia: Two participants from the LD group and one participant from the HC group were excluded from further analysis due to excessive motion during rsfMRI (mean relative motion > 0.25 mm).

Replication

The main experimental findings (Fig. 1b & Fig. 2) was replicated in the independent DBS-fMRI dataset (Extended Data Fig. 4), and the independent DBS-SS dataset (Extended Data Fig. 6 & Supplementary Fig. 3). The enlargements of the SCAN representations in the subcortical regions are in line with the cortical-subcortical hyperconnectivity in PD patients (Extended Data Fig. 5).
Moreover, we examined whether effective dopaminergic medication also normalizes SCAN hyperconnectivity. In a simplified levodopa challenge test, SCAN hyperconnectivity was significantly reduced by levodopa (Extended Data Fig. 8b).

Randomization

In the TMS study, 36 patients with PD (see Extended Data Table 1) were randomly divided into two groups at a ratio of 1:1, where one group received SCAN stimulation (SCAN group, n = 18) and the other M1 effector-specific stimulation (Effector group, n = 18), over a span of 14 consecutive days. The randomization codes were generated using a custom script by an independent research assistant before the start of the recruitment. The group allocation was kept in a sealed opaque envelope, which was only opened when a patient was enrolled. The assistant sent the target coordination according to the group allocation for each patient to TMS operators.
Randomization is not relevant to the other studies in this work because those components are observational neuroimaging or device on/off experimental designs rather than parallel-group interventions, random allocation was neither required nor applicable.

Blinding

In the TMS study, patients, assessors, TMS operators, and other research staff were all blinded to the group allocations.
Blinding was not relevant to the other studies because these components involved observational imaging analyses or fixed stimulation on/off conditions rather than investigator-driven treatment assignments. All participants underwent the same predefined procedures, and outcome measures were obtained objectively from imaging or electrophysiological data; therefore, blinding was neither required nor applicable.

Reporting for specific materials, systems and methods

We require information from authors about some types of materials, experimental systems and methods used in many studies. Here, indicate whether each material, system or method listed is relevant to your study. If you are not sure if a list item applies to your research, read the appropriate section before selecting a response.

Materials & experimental systems

n/a	Involved in the study
☒	☐ Antibodies
☒	☐ Eukaryotic cell lines
☒	☐ Palaeontology and archaeology
☒	☐ Animals and other organisms
☐	☒ Clinical data
☒	☐ Dual use research of concern
☒	☐ Plants

Methods

n/a	Involved in the study
☒	☐ ChIP-seq
☒	☐ Flow cytometry
☐	☒ MRI-based neuroimaging

Clinical data

Policy information about clinical studies

All manuscripts should comply with the ICMJE guidelines for publication of clinical research and a completed CONSORT checklist must be included with all submissions.

Clinical trial registration

NCT02937727; NCT06734676; NCT04002596; NCT03582891

Study protocol

Study overview is available online (NCT02937727: https://clinicaltrials.gov/study/NCT02937727?term=NCT02937727;&rank=1#study-overview; NCT06734676: https://clinicaltrials.gov/study/NCT06734676?term=NCT06734676:&rank=1#study-overview; NCT04002596:https://clinicaltrials.gov/study/NCT04002596?term=NCT04002596:&rank=1#study-overview; NCT03582891: https://clinicaltrials.gov/study/NCT03582891?term=NCT03582891:&rank=1#study-overview)

Data collection

NCT02937727: Data was collected at Tiantan Hospital, Beijing; Peking Union Medical College Hospital, Beijing; and Qilu Hospital, Jinan, China. Recruitment and data collection occurred between 2016-11 and 2018-03.
NCT06734676: Data was collected at Henan Provincial People's Hospital, China, from 2023-05 to 2024-05.
NCT04002596: Data was collected at Henan Provincial People's Hospital, China, from 2017-02 to 2020-08.
NCT03582891: Data was collected at the Departments of Neurology and Neurological Surgery at the University of California, San Francisco, from 2018-10 to 2024-06.

Outcomes

NCT02937727: The primary outcome is change in UPDRS part III [Time Frame: 1 month,3 months, 6 months and 12months] and

Outcomes	change in Local Field Potential Recordings using G106R [Time Frame: 1 month,3 months, 6 months and 12months]. Secondary outcome is change in UPDRS part III [Time Frame: 1, 3 months of stimulation], UPDRS part II [Time Frame: 1, 3 months stimulation], Levodopa Equivalent Dose [Time Frame: 1, 3 months stimulation], Drug Therapy are definied as levodopa equivalent dose,which is devodopa containing or dopamine agonist containing medications and Local Field Potential Recordings using G106R [Time Frame: 1 month, 3 months]. NCT06734676: The primary outcome is the difference in MDS-UPDRS-III scores at the "on" state at day 14 after iTBS intervention. NCT04002596: The primary outcome: (1) Primary effectiveness will be a comparison of the CRST scores at baseline vs. 3 months. (Range 0-152, scores are combined, the higher the score, the greater the clinical level of tremor, the worse clinical outcome is); (2) To evaluate the incidence and severity of adverse events (AEs) associated with the ExAblate Transcranial thalamotomy of medication-refractory, tremor dominant PD after the ExAblate treatment and during the follow-up period of up up to 1 year. The secondary outcome: (1) Clinical Rating Scale for Tremor, Total Score at 1year; (2) Clinical Rating Scale for Tremor, Part C at 1year; (3) Parkinson's Disease Questionnaire - 39 at 1 year. NCT03582891: The primary outcome: (1) duration of "on" stimulation time without dyskinesia from motor diaries in adaptive compared to standard open loop stimulation (Parkinson's disease patients). Comparison will use data from the testing of open and closed-loop stimulation during chronic adaptive DBS testing at home. (2) The Burke-Fahn-Marsden Dystonia Rating Scale-Movement aDBS testing compared to pre-operative baseline (Dystonia Patients). Comparison will use data from the testing of open and closed-loop stimulation during chronic adaptive DBS testing at home. (3) Toronto Western Spasmodic Torticollis Rating Scale during aDBS testing compared to pre-operative baseline (Dystonia Patients). Comparison will use data from the testing of open and closed-loop stimulation during chronic adaptive DBS testing at home. (4) Karolinska Sleepiness Scale: through study completion, up to 4 years. (5) Psychomotor vigilance task (PVT): through study completion, up to 4 years. (6) Positive and Negative Affect Schedule (PANAS-SF): Through study completion, up to 4 years.

Plants

Seed stocks	NA
Novel plant genotypes	NA
Authentication	NA

Magnetic resonance imaging

Experimental design

Design type	Resting-state fMRI
Design specifications	19 - 300 minutes of data per-participant
Behavioral performance measures	Behavioral outputs were not recorded.

Acquisition

Imaging type(s)	Structural (T1w and T2w) , Functional
Field strength	3.0 Tesla
Sequence & imaging parameters	PIPD: MRI was performed using a Siemens 3T Prisma MRI scanner equipped with a 64-channel head coil. The structural scans involved T1-weighted images acquired through a MP2RAGE sequence (TI1 = 755 ms, TI2 = 2500 ms, TE = 3.43 ms, TR = 5,000 ms, flip angle1 = 4°, flip angle2 = 5°, matrix size = 256 ×256, 208 sagittal slices, spatial resolution = 1 × 1 × 1 mm3). An acceleration factor of 3 (with 32 reference lines) was applied in the primary phase encoding direction, with online GRAPPA image reconstruction. Rs-fMRI data were acquired using a gradient-echo echo planar imaging (GE-EPI) sequence (TE = 35 ms, TR = 2,000 ms, flip angle = 80º, and 75 slices, spatial resolution = 2.2 × 2.2 × 2.2 mm3). During data acquisition, participants were instructed to maintain their eyes open, remain awake while keeping their body still, and minimize head movement. DBS-fMRI: All MRI data were collected using a 3T Philips Achieva TX whole-body MRI scanner equipped with a 32-channel head coil. T1-weighted structural images were acquired using a MPRAGE sequence, lasting 4 minutes and 14 seconds (TE = 3.70 ms, TR = 7.52 ms, flip angle = 8°, 180 sagittal slices, spatial resolution = 1 × 1 × 1 mm³). Functional images were acquired with a 6-minute and 14-second transversal GE-EPI sequence (TE = 30 ms, TR = 2000 ms, flip angle = 90°, 37 slices, spatial resolution = 2.875 × 2.875 × 4 mm³, 184 frames/run). CT images were acquired with a uCT 760 (United Imaging, Shanghai) scanner one month after surgery. A head helical sequence, with FOV = 512×512, pixel spacing = 0.449 mm × 0.449 mm, 204 slices, slice thickness = 0.625 mm, was used. TMS: MRI was performed using a Siemens 3T Prisma MRI scanner equipped with a 64-channel head coil. The structural scans involved T1-weighted images acquired through a MP2RAGE sequence (TI1 = 755 ms, TI2 = 2500 ms, TE = 3.43 ms,

TR = 5,000 ms, flip angle1 = 4°, flip angle2 = 5°, matrix size = 256 ×256, 208 sagittal slices, spatial resolution = 1 × 1 × 1 mm3). An acceleration factor of 3 (with 32 reference lines) was applied in the primary phase encoding direction, with online GRAPPA image reconstruction. Rs-fMRI data were acquired using a gradient-echo echo planar imaging (GE-EPI) sequence (TE = 35 ms, TR = 2,000 ms, flip angle = 80º, and 75 slices, spatial resolution = 2.2 × 2.2 × 2.2 mm3). During data acquisition, participants were instructed to maintain their eyes open, remain awake while keeping their body still, and minimize head movement.
MRgFUS: MRI was performed using a Siemens 3T Prisma MRI scanner equipped with a 64-channel head coil. The structural scans involved T1-weighted images acquired through a MP2RAGE sequence (TI1 = 755 ms, TI2 = 2500 ms, TE = 3.43 ms, TR = 5,000 ms, flip angle1 = 4°, flip angle2 = 5°, matrix size = 256 ×256, 208 sagittal slices, spatial resolution = 1 × 1 × 1 mm3). An acceleration factor of 3 (with 32 reference lines) was applied in the primary phase encoding direction, with online GRAPPA image reconstruction. Rs-fMRI data were acquired using a gradient-echo echo planar imaging (GE-EPI) sequence (TE = 35 ms, TR = 2,000 ms, flip angle = 80º, and 75 slices, spatial resolution = 2.2 × 2.2 × 2.2 mm3). During data acquisition, participants were instructed to maintain their eyes open, remain awake while keeping their body still, and minimize head movement.T2w scans were collected the day after the MRgFUS intervention to image the brain lesions, using a 3T MRI scanner (Discovery MR750, GE Healthcare, Milwaukee, USA) equipped with an 8-channel head coil (axial scans, TE = 98 ms, TR = 6279 ms, flip =111°, matrix = 288 × 384, FOV = 240 × 240 mm, slice thickness = 2 mm, slice interval = 2mm, 31 slices; coronal scans, TE = 98 ms, TR = 6264 ms, flip = 111°, FOV = 240 × 240mm, matrix = 224 × 384, slice thickness = 2mm, slice interval = 2mm, 25 slices; sagittal scans, TE = 98 ms, TR = 6268 ms, flip = 111°, FOV = 240 × 240mm, matrix = 288 × 384, slice thickness = 2mm, slice interval = 2mm, 31 slices).
LCT: All MRI data were acquired using a 3T GE SIGNA UHP scanner equipped with a 48-channel head coil at Changping Laboratory. In the medication OFF state (≥12 hours after medication withdrawal), five rsfMRI runs (6 minutes each, totaling 30 minutes) were acquired with a gradient-echo EPI sequence (TR = 3000 ms, TE = 30 ms, flip angle = 90°, voxel size = 3 × 3 × 3 mm^3, 47 axial slices). After the medication OFF scanning, the patient was instructed to take 150% of their regular morning levodopa dose by a neurologist from the Peking University First Hospital, and once peak motor response was jointly confirmed by the patient and the evaluator, the medication ON scan was conducted using the same imaging protocol. Subsequently, structural images were collected using a 3D MPRAGE T1-weighted sequence with 1 mm isotropic resolution (192 sagittal slices, TR = 2708 ms, TE = 3.5 ms, TI = 900 ms, flip angle = 8°, FOV = 256 × 256 mm^2). During all MRI sessions, participants were instructed to keep their eyes closed, remain awake, minimize head motion, and stay as still as possible.
ET: MRI was performed using a Siemens 3T Prisma MRI scanner equipped with a 64-channel head coil. The structural scans involved T1-weighted images acquired through a MP2RAGE sequence (TI1 = 755 ms, TI2 = 2500 ms, TE = 3.43 ms, TR = 5,000 ms, flip angle1 = 4°, flip angle2 = 5°, matrix size = 256 ×256, 208 sagittal slices, spatial resolution = 1 × 1 × 1 mm3). An acceleration factor of 3 (with 32 reference lines) was applied in the primary phase encoding direction, with online GRAPPA image reconstruction. Rs-fMRI data were acquired using a gradient-echo echo planar imaging (GE-EPI) sequence (TE = 35 ms, TR = 2,000 ms, flip angle = 80º, and 75 slices, spatial resolution = 2.2 × 2.2 × 2.2 mm3). During data acquisition, participants were instructed to maintain their eyes open, remain awake while keeping their body still, and minimize head movement.
Dystonia: Participants underwent one structural MRI scan, and four rsfMRI scans, each spanning 6 minutes, resulting in a cumulative scan duration of 20 minutes. MRI data were acquired using a 3T Siemens Magnetom Prisma fit scanner equipped with a 32-channel head coil (Siemens Healthineers, Forchheim, Germany). T1-weighted structural imaging used a 3D MPRAGE sequence (TR=2.5s, TI=1.0s, 0.8mm isotropic voxels, FoV=256mm, 208 sagittal slices, flip angle=8°, bandwidth=740Hz/Px). RsfMRI were obtained with a GE-EPI sequence (TR=3000ms, TE=30ms, 3.0mm isotropic voxels, FoV=216mm, 47 sagittal slices, flip angle=85°, bandwidth=2240Hz/Px, echo spacing=0.51ms). During the resting-state scans, participants were instructed to remain still with their eyes closed, stay awake, and relax without focusing on any specific thoughts.
ALS: All MRI data were acquired using a 3T GE SIGNA UHP scanner equipped with a 48-channel head coil. Five rsfMRI runs (6 minutes each, totaling 30 minutes) were acquired with a gradient-echo EPI sequence (TR = 3000 ms, TE = 30 ms, flip angle = 90°, voxel size = 3 × 3 × 3 mm^3, 47 axial slices). Structural images were collected using a 3D MPRAGE T1-weighted sequence with 1 mm isotropic resolution (192 sagittal slices, TR = 2708 ms, TE = 3.5 ms, TI = 900 ms, flip angle = 8°, FOV = 256 × 256 mm^2). During all MRI sessions, participants were instructed to keep their eyes closed, remain awake, minimize head motion, and stay as still as possible.

Area of acquisition: Head/Brain

Diffusion MRI ☐ Used ☒ Not used

Preprocessing

Preprocessing software: The processing of both rs-fMRI and structural data was conducted using the personalized Brain Functional Sectors (pBFS) Cloud v1.0.7 (Neural Galaxy Inc., Beijing). The fMRI preprocessing sequence encompassed the following steps: (1) slice timing correction through stc_sess from the FreeSurfer version 6.0.0 software package (http://surfer.nmr.mgh.harvard.edu), (2) head motion correction using mc_sess from FreeSurfer (https://surfer.nmr.mgh.harvard.edu/fswiki/mc-sess), (3) linear detrending and bandpass filtering within the range of 0.01-0.08 Hz, and (4) regression to account for nuisance variables, which encompassed the six motion parameters, white matter signal, ventricular signal, global signal, and their first-order temporal derivatives. For MP2RAGE T1w images of the PIPD, TMS, and MRgFUS dataset, the brain was first extracted from the uniform T1-weighted image using Advanced Normalized Tools (ANTs). The subsequent preprocessing steps are consistent across structural sequences from the three datasets. The FreeSurfer version 6.0.0 software package (http://surfer.nmr.mgh.harvard.edu) was employed for processing. Surface mesh representations of the cerebral cortex were reconstructed from T1w images and non-linearly aligned to a shared spherical coordinate system. The functional and structural images were coregistered using boundary-based affine registration from the FsFast software package (http://surfer.nmr.mgh.harvard.edu/fswiki/FsFast).

Normalization: For the surface preprocessing pipeline, the functional images were aligned with the FreeSurfer cortical surface template (fsaverage6, 40,962 vertices per hemisphere).
For the volumetric preprocessing pipeline, the preprocessed functional images in native space were normalized to a 2-mm

spatial resolution volumetric template (the FSL-version of the MNI ICBM152 nonlinear template) using a co-registration matrix and volumetric nonlinear registration with ANTs.

Normalization template

Surface: fsaverage6, 40,962 vertices per hemisphere
volumetric : FSL-version of the MNI ICBM152 nonlinear template

Noise and artifact removal

Additional confound analyses: regression to account for nuisance variables, which encompassed the six motion parameters, white matter signal, ventricular signal, global signal, and their first-order temporal derivatives.

Volume censoring

NA

Statistical modeling & inference

Model type and settings

Independent t-tests were employed to evaluate the differences between two independent groups, while paired t-tests were used to compare means from the same group at two different time points or conditions.
Chi-square tests were conducted to examine the distribution of responsive electrodes within the SCAN and effector regions.
Linear Mixed Effects (LME) models were applied to analyze longitudinal data, accounting for the effects of time and individual differences.
Spearman correlation coefficients were utilized to assess the correlation between the Euclidean distances of the treatment targets and motor symptom improvement.
Permutation tests, including cluster-based permutation tests, were conducted to evaluate statistical significance without assuming a specific distribution and to control the false discovery rate. The Dice coefficient was used to measure the overlap between the volume of tissue activated (VTA) and the targeted sub-cortical structures.
Additionally, FDR corrections were implemented to manage the error rates associated with multiple comparisons.

Effect(s) tested

see above

Specify type of analysis: ☐ Whole brain ☐ ROI-based ☒ Both

Anatomical location(s)

The following altas-based sub-cortical parcellations were used:
The DISTAL atlas is available at https://www.lead-dbs.org/helpsupport/knowledge-base/atlasesresources/distal-atlas/; The HybraPD atlas is available at https://www.lead-dbs.org/helpsupport/knowledge-base/atlasesresources/atlases-2/
The effective DBS lead locations(DBS-SS) within the STN, GPi, and VIM was recored in Supplementary Table 1.

Statistic type for inference

No cluster wise inferences were made.

(See Eklund et al. 2016)

Correction

Multiple comparisons were controlled using FDR correction.

Models & analysis

n/a	Involved in the study
☐	☒ Functional and/or effective connectivity
☒	☐ Graph analysis
☐	☒ Multivariate modeling or predictive analysis

Functional and/or effective connectivity

Resting-state functional connectivity was estimated by Pearson's correlation coefficient of BOLD-fMRI signals

Multivariate modeling and predictive analysis

To take advantage of the longitudinal DBS-fMRI dataset with multiple follow-up timepoints for each participant, we used two LME models to evaluate the DBS long-term effects on motor symptoms and RSFC. The UPDRS-III score served as the dependent variable, with follow-up timepoints defined as a fixed effect, and participant identity as a random effect. Post-hoc pairwise t-tests were conducted to compare the pre-operative scores and the post-operative scores.Similarly, an LME model was employed to evaluate the changes in RSFC of the SCAN circuit.
Additionally, an LME model was used to investigate the relationship between changes in clinical outcomes and STN-SCAN RSFC across different follow-up visits. The dependent variable was the observed change rate in UPDRS-III scores, while the fixed effects included the change rate of STN-SCAN RSFC and the follow-up timepoints, also participant was considered as a random effect.
In the TMS study, an LME model was employed to assess the effects on motor symptoms of different stimulation targets on score changes across all clinical assessments. Fixed effects included stimulation target group, time of assessment , and their interaction, with disease duration, levodopa equivalent dose (LEDD) and baseline Hoehn and Yahr staging as covariates. Participant identification was the random effect.